Submarine Seakeeping and Resistance in Irregular Waves

Saleh Aminia, Mahmoud Rostami Varnousfaaderanib, Mojtaba Dehghan Manshadic, Hossein Norouzid

This study presents numerical simulations of submarine motion near the free water surface in the presence of irregular waves, with results compared to calm water conditions. Using the URANS method, the amplitudes of the submarine's heave, pitch, and roll motions were calculated. The hydrodynamic behavior of the submarine was analyzed with STAR-CCM+ in both surface and submerged modes near the free surface. The effects of encounter angles and varying wave characteristics on the amplitude of submarine motions were also investigated. The results show that the largest amplitudes of pitch and heave motions occur in following waves, while the highest amplitude of roll motion is observed in beam waves. Additionally, following waves exhibit the lowest frequency of motion oscillation. In surface mode, due to the increased height of the longitudinal metacenter compared to submerged mode, the amplitude of pitch motions is reduced. However, in surface mode, the stability of the transverse metacenter and the increased influence of wave effects on the free surface lead to greater roll motion amplitudes. The increase in residual resistance in surface mode.

KEY WORDS

- ~ Suboff submarine
- ~ Heave
- ~ Pitch
- ~ Roll
- ~ Irregular waves
- ~ URANS method

Malek-Ashtar University of Technology, Faculty of Mechanical Engineering, Isfahan, Iran

e-mail: rostamivf@aut.ac.ir doi: 10.7225/toms.v14.n03.005

Received: 3 Nov 2024 / Revised: 28 Mar 2025 / Accepted: 7 Jul 2025 / Published: 21 Oct 2025

This work is licensed under



1. INTRODUCTION

In recent years, many researchers have investigated the hydrodynamic behavior of vessels and underwater vehicles using CFD due to the high costs of experimental testing and advancements in computational power. Li et al. (2021) studied the hydrodynamic behavior of submarines near the water's free surface using CFD. Their findings revealed that hydrodynamic coefficients change significantly as the submarine approaches the free surface, while these changes diminish with increasing immersion depth. Additionally, variations in velocity and phase differences between wave systems affect the surface wave height and wavelength. Carrica et al. (2019) simulated the Joubert submarine near the water's free surface using an overset grid technique with control surfaces and a propeller. Their simulations, conducted at different depths in calm water and regular waves under sea states 2 to 7, demonstrated excellent agreement with experimental data, even with a coarse grid. The study showed that operating near the free surface generates significant vertical forces and torques, which increase propeller thrust and reduce efficiency. Moreover, moment and thrust coefficients were observed to decrease with increasing velocity. Amiri et al. (2018, 2019, 2020), Nematollahi et al. (2015), and Ling et al. (2022) explored the hydrodynamic behavior of underwater vehicles under free surface effects using the URANS method. They analyzed the effects of immersion depth on performance. Their results revealed that motion-induced waves generated by the submerged vehicle form distinct wave patterns. Furthermore, lift forces, pitch moments, and drag forces on the submarine increase as it approaches the free surface, with these effects diminishing at greater depths. The studies also found that hydrodynamic coefficients are influenced by wave characteristics, and the free surface effect rapidly decreases with increasing immersion depth. Dong et al. (2022) conducted simulations of the Suboff submarine under free surface conditions using the URANS method. Their research investigated the effects of depth and irregular waves on submarine hydrodynamic behavior. The results indicated that approaching the free surface leads to an increase in moment, drag, and lift forces.

Saout and Ananthakrishnan (2011) examined the stability of a submarine moving near the free surface of the water using the planar motion mechanism. Their results, compared with those at fully submerged depths, indicated that the absence of a free surface near the submarine eliminates unsustainable oscillating velocities. They also identified the locations of the fins and the center of mass within the submarine as critical factors influencing its stability during motion. Wilson-Haffenden et al. (2009) experimentally studied the impact of the free surface on the resistance, lift, and moments of an underwater vehicle. Their findings revealed that the free surface significantly affects wave drag and the dynamic pressure distribution along the length of the vehicle, while also increasing the pitch moment and lift force on the submarine. Jagadeesh and Murali (2010), Mansoorzadeh and Javanmard (2014), and Nematollahi et al. (2015) investigated the free surface effects on submarine behavior using URANS equations. Their validations confirmed the reliability of URANS equations in determining hydrodynamic coefficients. They observed that drag force increases with decreasing immersion depth due to the dynamic pressure component. Tian et al. (2019) conducted numerical modeling of an AUV without attachments operating close to the free surface. Their study, which considered a stationary submarine under regular waves, demonstrated that hydrodynamic coefficients exhibit regular oscillations. The oscillation amplitude increased with higher wave amplitudes, lower Reynolds numbers, and shallower immersion depths. The oscillations of hydrodynamic coefficients were found to correlate with the peaks and oscillations of the wave pattern. Wang et al. (2020) performed experimental and numerical simulations of an autonomous submarine operating near the free surface. Their study focused on vortices and wake patterns, confirming the reliability of their numerical method through comparison with experimental results. Han et al. (2021) employed CFD to investigate the maneuvering behavior of the Joubert BB2 submarine. Their findings highlighted that rotational motions have a greater influence on the pitch moment and lift forces of the submarine. The planar motion mechanism was used in this analysis. Qi et al. (2018) explored the effects of irregular waves and varying depths on the hydrodynamic behavior of submarines operating near the free surface using the URANS method.

Their results confirmed that drag, moment, and lift forces increase as the submarine approaches the free surface. However, the study limited the submarine's freedom of motion. Shariati and Mousavizadegan (2017) analyzed the effect of attachments on the hydrodynamic characteristics of the Suboff submarine near the water surface. Their results focused on variations in drag force and wave patterns. Kim (2011) investigated submarine stability near the free surface using CFD, with particular attention to changes in hydrodynamic coefficients.

In the aforementioned studies, the submarine is analyzed without considering freedom of motion. Investigating the seakeeping behavior of surface vessels under the influence of surface waves is crucial, leading to numerous studies in recent years. Jiao and Huang (2020), Kim et al. (2022), Ozturk et al. (2021), Huang et al. (2021) conducted numerical simulations to evaluate the seakeeping performance of vessels. Bi et al. (2019), Sun et al. (2017) focused on SWATH vehicles, examining the impact of wave and body characteristics on the hydrodynamic behavior of floats. Similarly, Liao et al. (2021), Su et al. (2021) analyzed the seakeeping performance of trimarans, with their findings demonstrating strong agreement with experimental results, thereby confirming the reliability of numerical methods for seakeeping analysis. Due to their higher accuracy compared to strip theory and potential function methods—especially for predicting roll motions—the URANS method has been widely adopted in recent research. Previous methods, such as strip theory, often lack accuracy in calculating floating responses as they neglect viscosity and turbulence effects. Modern studies predominantly utilize the Finite Volume Method (FVM¹) for discretizing equations, the SIMPLE² algorithm for coupling velocity and pressure equations, and the DFBI³ module for dynamic body interaction. These simulations are typically performed in regular or irregular waves using the RANS-VOF⁴ solver with the overset grid approach.

Although most sea conditions involve irregular waves, a review of previous studies reveals that submarine motion has rarely been investigated under such conditions. This highlights the importance of studying submarine hydrodynamic behavior in the presence of irregular waves. Additionally, the freedom of motion of a submarine has received limited attention in prior research. In this study, the amplitude of motions is calculated numerically in irregular waves and compared with calm water conditions. The seakeeping performance and resistance force of the submarine are analyzed with coupled heave, pitch, and roll (HPR) motions. Simulations are conducted for different wave specifications and encounter angles. Furthermore, the results are compared at two different depths: one in surface mode (dimensionless depth of 0.25) and one in submerged mode (dimensionless depth of 1.1). A total of 22 simulations are performed.

This paper presents a comprehensive computational fluid dynamics simulation, using STAR-CCM+, of submarine hydrodynamic behavior in irregular waves. The study is organized as follows: Section 2 outlines the model geometry, governing equations, and simulation setup. Section 3 details the simulation conditions. Validation and verification are discussed in Section 4. Section 5 provides a seakeeping analysis, including results and discussion. This analysis covers a detailed investigation of the motion response and resistance force of the submarine under various irregular wave conditions and encounter angles. Finally, Section 6 summarizes the key conclusions of the study.

3

¹ Finite Volume Method

² Semi-Implicit Method for Pressure Linked Equations

³ Dynamic Fluid Body Interaction

⁴ Volume Of Fluid

2. MATHEMATICAL AND NUMERICAL MODEL

2.1 Governing Equations

In this paper, the URANS method was employed as the primary approach for the simulations. The continuity and momentum equations used in the study are presented below (Ferziger et al., 2019):

$$\frac{\partial \rho}{\partial t} + \frac{\partial}{\partial x_i} (\rho u_i) = 0 \qquad i = 1, 2, 3 \tag{1}$$

$$\frac{\partial}{\partial t}(\rho \bar{u}_i) + \frac{\partial}{\partial x_i}(\rho \bar{u}_i \bar{u}_j) = F_i - \frac{\partial p}{\partial x_i} + \frac{\partial \tau_{ij}}{\partial x_j} + \rho g_i$$

$$\tau_{ij} = \mu \left(\frac{\partial \bar{u}_i}{\partial x_i} + \frac{\partial \bar{u}_j}{\partial x_i}\right) - \frac{2}{3} \delta_{ij} \frac{\partial \bar{u}_i}{\partial x_i} \qquad i, j = 1, 2, 3$$
(2)

In which ρ denotes fluid density, u indicates fluid velocity, μ indicates the dynamic viscosity, p indicates static pressure, F_i indicates body forces and $\overline{u_i}\overline{u_j}$ denotes Reynolds stress tensor. Using the Boussinesq model, the Reynolds stress tensor is calculated as follows:

$$\rho \overline{u_i' u_j'} = -\mu_t \left(\frac{\partial u_i}{\partial x_j} + \frac{\partial u_j}{\partial x_i} \right) + \frac{2}{3} \delta_{ij} k$$

$$\mu_t = \rho C_u k^2 / \varepsilon$$
(3)

The k- ε turbulence model has been used to simulate the turbulent flow around the body (Lateb et al., 2013). Where ε is the dissipation rate, μ_t denotes the eddy viscosity, k denotes the turbulent kinetic energy, C_{μ} denotes an empirical constant and δ representes Kronecker delta. ε and k are then calculated from the k- ε realizable employing two transport equations.

The VOF¹ method is applied to track the interface between water and air. This method is defined by the following equation:

$$\frac{\partial \alpha}{\partial t} + u_i \frac{\partial \alpha}{\partial x_i} = 0 \tag{4}$$

The volume fraction function α is defined between 0 to 1. If the computational cell contains full air, $\alpha=0$, and if the calculational cell contains full water, $\alpha=1$. In each cell, the density and viscosity are obtained as follows (Lee et al., 2019):

$$\rho = \rho_w \alpha + \rho_a (1 - \alpha)$$

$$\mu = \mu_w \alpha + \mu_a (1 - \alpha)$$
(5)

¹ Volume Of Fluid

To prevent wave reflection at the end of the computational domain, a wave damping area is applied. In this region, waves are attenuated by introducing resistance to vertical motion (Choi and Yoon, 2009).

$$S_z = \rho(f_1 + f_2|w|) \frac{e^{k-1}}{e-1} w$$

$$k = \left(\frac{x - x_{Sd}}{x_{ed} - x_{Sd}}\right)^n$$

$$|x_{ed} - x_{Sd}| = \lambda_{max}$$
(6)

In this equation, f_1 , f_2 and n represent the constant parameters of the damping model. x_{ed} denotes the endpoint of the wave damping area, x_{Sd} represents the starting point of the wave damping area, and w indicates the vertical velocity.

2.2 Submarine Geometry

The DARPA SUBOFF autonomous underwater vehicle is selected for the simulations in this paper (Groves et al., 1989). For validation, a bare hull with a scale ratio of 1:2.8 was utilized, while a full-appendage model with a scale ratio of 1:1 was employed for simulations. Figure 1 illustrates the full appendages and bare hull of the DARPA SUBOFF model.

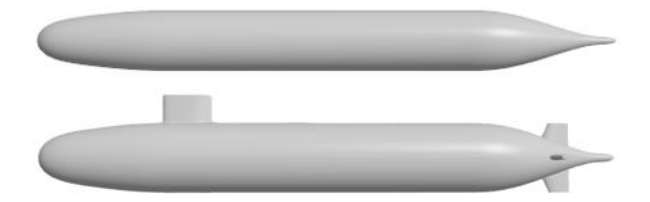


Figure 1. Fully appendages and bare hull Darpa Suboff submarine model.

The length-to-diameter ratio of the model is $\frac{L}{D}$ =8.575. Table 1 presents the principal characteristics of the submarine model, where x_{CG} represents the longitudinal center of gravity measured from the nose of the submarine, and z_{CG} indicates the distance between the vertical center of gravity and the centerline of the parallel part of the submarine. The body-fixed coordinate system is defined at the center of gravity and within the plane of symmetry of the submarine. The negative x-axis points toward the submarine's nose, while the positive z-axis is directed toward the water's free surface.

Dringing particulars of SUDOFF	Fully appendage	Bare hull	
Principal particulars of SUBOFF	Full scale	model	
Scale	1:1	1:2.8	
m(kg)	525.024	31.31	
A (m ²)	6.3343	0.7571 0.03138	
$\nabla(m^3)$	0.05262		
x _{cb} (m)	2.013	0.7167	
z _{CG} (m)	-0.05	0	
Overall Length (mm)	4.356	1.551	
Diameter (m)	0.508	0.181	
Parallel Part Length (m)	2.229	0.366	
Bow Part Length (m)	1.016	0.324	
Stern Part Length (m)	1.111	0.861	

Table 1. Principal characteristics of the Darpa Suboff submarine.

2.3 Numerical Simulation setup

The motion of the submarine in waves is an unsteady action. Simulation of the flow around the submarine body is done by the URANS method using STAR-CCM+. Compared to experimental methods, strip theory, and the potential function method, the URANS equation offers an optimal balance between computational accuracy and cost. In this study, transient three-dimensional CFD simulations were conducted to assess the performance of the AUV under the influence of wave and gravity effects (Liao et al., 2021, Huang et al., 2021, Jiao and Huang, 2020, Shivachev et al., 2020). The VOF method, combined with the HRIC scheme, was employed to accurately capture the free surface between air and water (Hirt and Nichols, 1981).

The solver employs the finite volume method (FVM) to discretize the transport equations across the entire domain. For temporal discretization of the transient terms, a second-order implicit backward Euler scheme was used. Spatial discretization utilized a second-order centered scheme for the diffusive terms and a second-order upwind numerical scheme for the convective terms. The SIMPLE algorithm was applied to

¹ High-Resolution Interface Capturing

couple the pressure-velocity equations effectively. The DFBI¹ module was employed to simulate the motion of a rigid body in response to external forces.

One of the factors influencing the computational domain is the turbulence model selected for numerical simulation. The choice is determined by the requirements of the first grid cell in relation to the turbulence model. For numerical simulations of two-phase flows involving curved surfaces, the "k- ϵ Realizable" turbulence model is commonly used. This model provides a good balance between accuracy, computational cost, and robustness. In this study, the "k- ϵ Realizable" turbulence model was employed (Tian et al., 2019, Nematollahi et al., 2015).

A high Y+ wall treatment was used as the wall function approach, based on the equilibrium turbulent boundary layer theory. The dimensionless Y+ value, which depends on the turbulence model, should fall between 30 and 100 for the $"k-\varepsilon"$ model. As shown in Figure 2, the Y+ values within this range demonstrate the accuracy of the grid at the wall boundary.

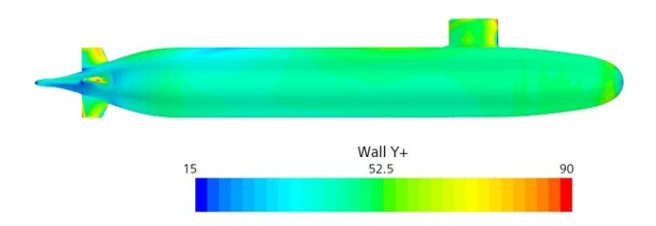


Figure 2. Y+ on the boundary of the wall.

Modeling an object involves defining its geometry, determining boundary conditions, and specifying domain dimensions to ensure the validity of the results. Selecting appropriate domain dimensions and boundary conditions, along with accurate grid generation and numerical settings aligned with the physics of the problem, ensures precise outcomes.

To simulate submarine motions in irregular waves, a cuboid tank was selected as the computational domain. The domain size must be sufficiently large to prevent boundary effects from influencing the flow around the body. However, increasing domain dimensions leads to higher cell counts and, consequently, increased computational costs. Therefore, the minimum domain dimensions that prevent boundary effects on the flow were determined. The dimensions are 28 (m) in length, 12 (m) in width, and 15 (m) in height (5 (m) for air and 10 (m) for water) (Ling et al., 2022, Shariati and Mousavizadegan, 2017). To ensure the accuracy of the results, the dimensions of the computational domain are larger than the ITTC (2011) recommendations. Therefore, better simulation results are expected. The wave damping area is added to the end of the computational domain to prevent the wave from returning, with its length approximately one wavelength for each simulation (Amiri et al., 2020). Additionally, a domain independence study has been conducted, confirming that the results are independent of the domain size, which ensures both the accuracy of the results and a reduction in computational time and cost.

2.4 Simulation conditions

The simulations were conducted in irregular waves, and the results were compared across various wave conditions. Additionally, different encounter angles and depths were analyzed. Figure 3 illustrates the

¹ Dynamic Fluid Body Interaction

location of the submarine in the simulations under irregular head waves. The simulations were performed at two distinct depths: surface mode (dimensionless depth of 0.25) and submerged mode (dimensionless depth of 1.1). The dimensionless depth is calculated as follows:

$$D^* = \frac{h}{D} = 0.25, 1.1$$

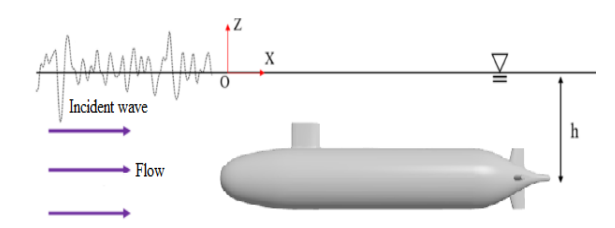


Figure 3. Submarine in the simulation.

The JONSWAP wave spectrum was utilized to generate irregular waves (Hou and Zou, 2016, Lau et al., 2022). For irregular waves, the ratio of the peak period of the wave to the significant wave height is recommended as follows (CD-adapco, 2020):

$$3.6 < \frac{T_P}{\sqrt{h_s}} < 5 \tag{7}$$

Which h_s denotes the significant wave height and T_P denotes the peak wave period. This relationship, by controlling the wave slope, prevents wave breaking. Additionally, this ratio is maintained constant in all generated waves.

Froude number will be constant in all simulations. The simulation time in the irregular wave is determined as follows, which \overline{T} denotes the average period and N denotes the number of waves. Hence, the physical time for each simulation is about 100 seconds.

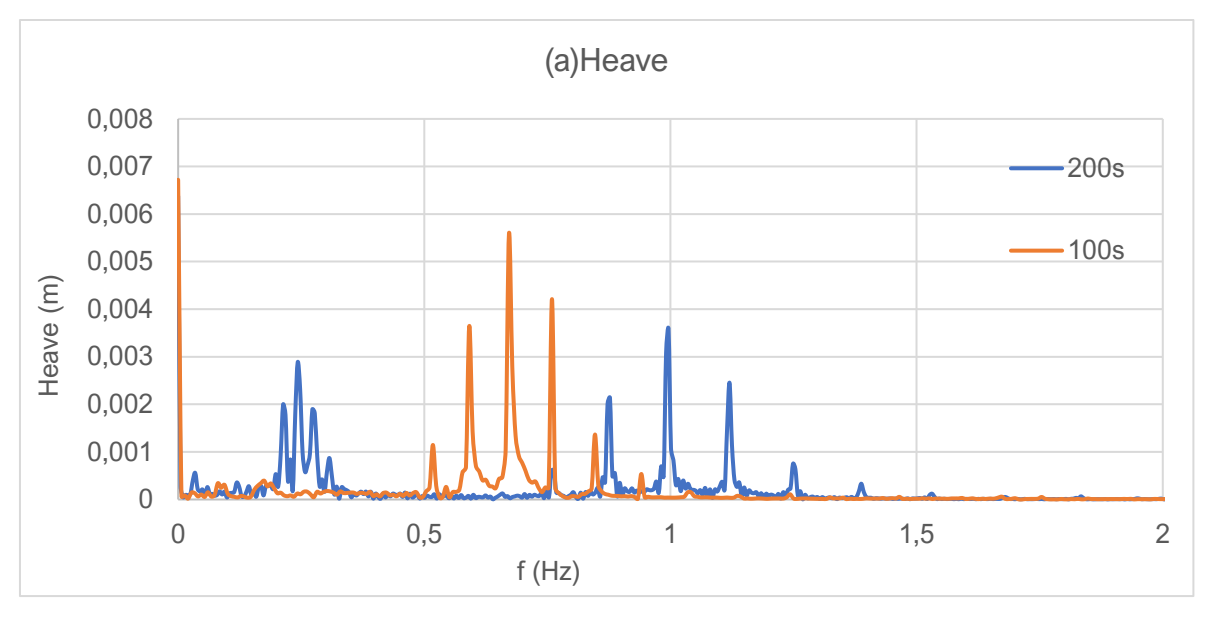
$$T_{Ph} \cong N \times \bar{T} \tag{8}$$

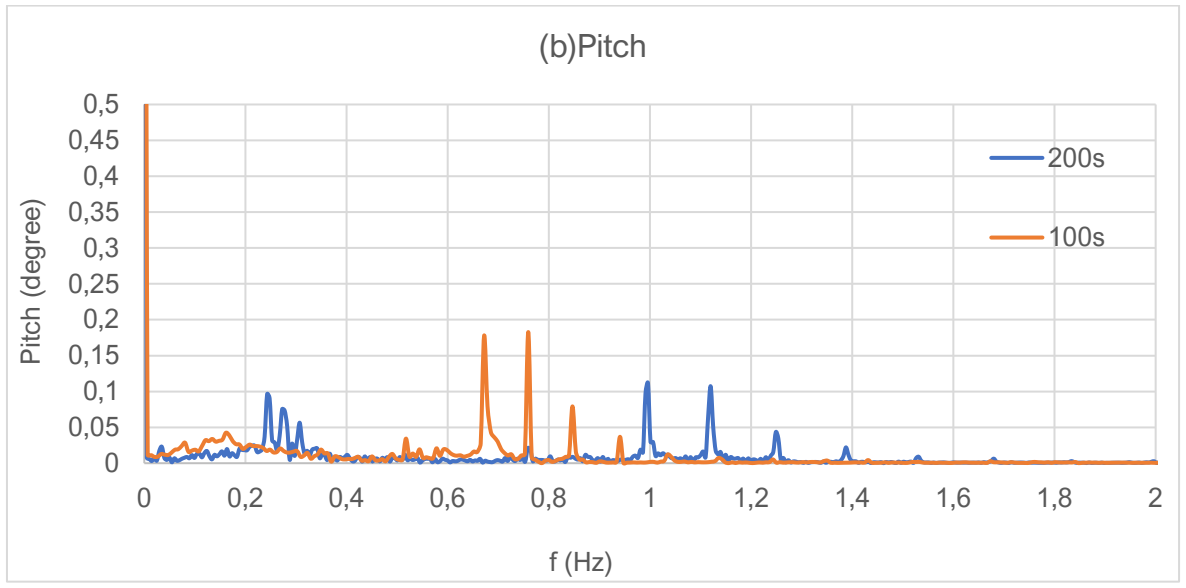
Using this approach, a simulation time of approximately 100 seconds was calculated, which is sufficient to include multiple wave periods and capture statistically meaningful hydrodynamic responses. Additionally, this approach helps reduce the computational cost and time while maintaining the accuracy and reliability of the results.

To assess the statistical reliability of motion responses in irregular wave conditions, the impact of simulation duration was investigated. While longer simulations can offer reduced statistical variability, they significantly increase computational demands, especially for CFD approaches based on the URANS method. In this study, each 100s simulation required approximately eight days of computation, limiting the feasibility of longer runs across multiple cases. Therefore, due to the computational demands of URANS simulations, most similar studies in the literature are also limited to durations of approximately 100s (Gao and Shi, 2023, Zan et al., 2025, Zhang et al., 2024).

To evaluate the adequacy of the selected duration, one representative case was extended to 200s. The analysis was conducted under irregular wave conditions, characterized by a significant wave height of 0.08 m, a peak period of 1.75 s, a non-dimensional water depth of 0.25, and a Froude number of 0.3146. The comparison of results, presented in Figure 4, shows that the heave, and pitch, roll response spectra exhibit a

slight increase in peak amplitude for the shorter duration. However, the dominant frequency range remains nearly unchanged. The comparison between 100 and 200s simulations shows that increasing the duration helps reduce statistical fluctuations and smooth out the response spectra. However, the overall patterns and key dynamic features remain consistent across both durations for all motions and mean resistance. This suggests that the 100s simulation provides sufficiently reliable results while significantly reducing computational cost.





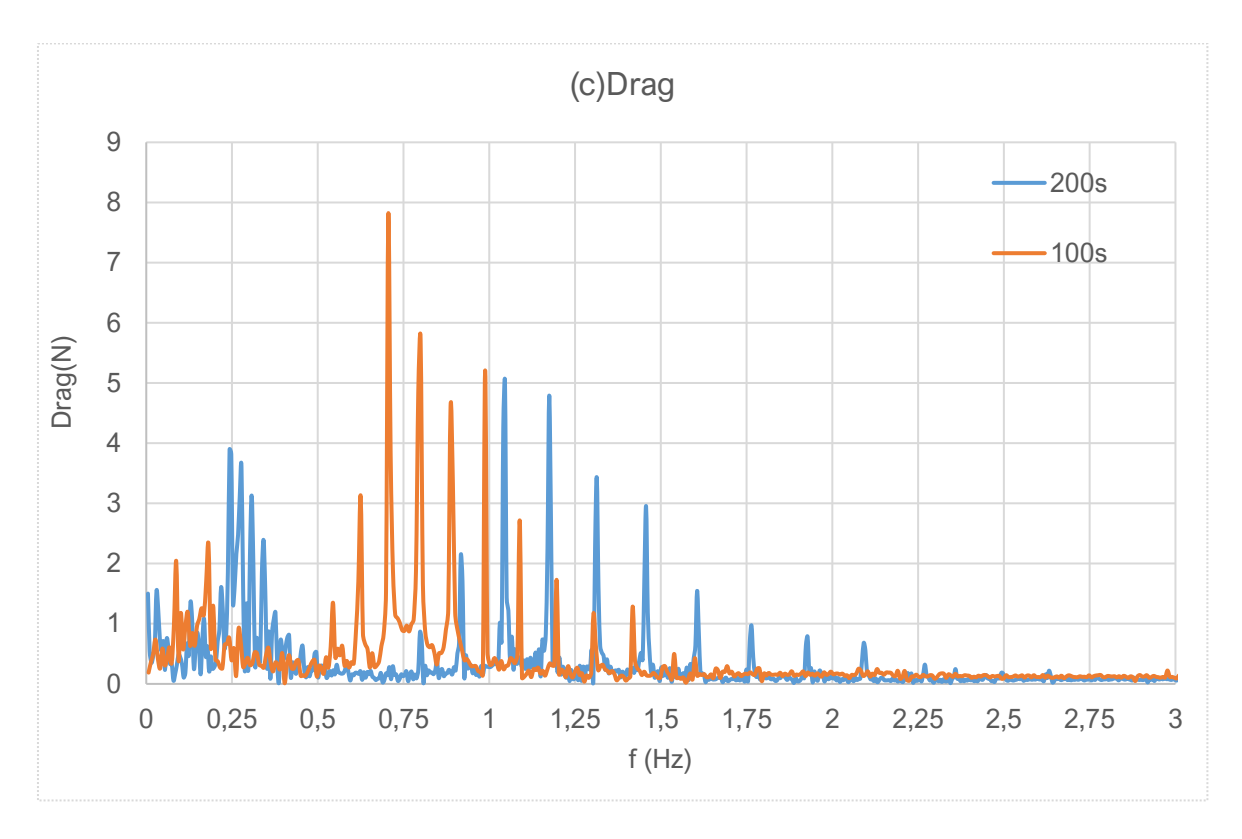


Figure 4. Response spectra of (a) heave, (b) pitch and (c) drag for both simulation durations.

Additionally, as presented in Table 1, heave, and pitch motions exhibit minimal variation between the two simulation durations, with comparable mean drag values also observed. These observations confirm that a simulation duration of 100s is sufficient to capture representative motion behavior with acceptable accuracy. The URANS approach, due to its ability to resolve viscous and turbulent flow features more comprehensively, also facilitates faster convergence of motion amplitudes compared to lower-order methods, supporting the robustness of the chosen simulation duration.

Duration (s)	Heave Max (m)	Heave RMS (m)	Pitch Max (deg)	Pitch RMS (deg)	Mean drag (N)
100	-0.02159	0.007374	1.6685	0.883434	154.0635
200	-0.02159	0.007456	-1.6685	0.881048	154.0635

Table 2. Comparison of maximum and RMS amplitudes of motions, and mean drag across both simulation durations.

Different simulation cases are presented in Table 2. Simulations have been conducted in both surface mode ($D^* = 0.25$) and submerged mode (($D^* = 1.1$) for irregular waves with varying significant heights and three different heading angles: 0° (following wave), 180° (head wave), and 90° (beam wave). In all simulation cases, the Froude number remains constant. Due to the symmetry of the geometry in the X-Y-planes, the results for a 90° angle will be identical to those for a 270° angle.

Case number	Wave direction (°)	Degree of Freedom	D*	(m)h _s	$(s)T_P$	Froude number
1, 2	flat	0 DOF, HPR	0.25	-	-	0.3146
3, 4, 5, 6, 7, 8, 9, 10, 11	180, 90, 0	HPR	0.25	0.43, 0.465, 0.5	2.361, 2.455, 2.55	0.3146
12, 13	flat	0 DOF, HPR	1.1	-	-	0.3146
14, 15, 16, 17, 18, 19, 20, 21, 22	180, 90, 0	HPR	1.1	0.43, 0.465, 0.5	2.361, 2.455, 2.55	0.3146

Table 3. Conditions of different simulation cases.

In this paper, the submarine's course direction was kept constant, while the direction of wave propagation for the incident waves was varied, as shown in Figure 4.

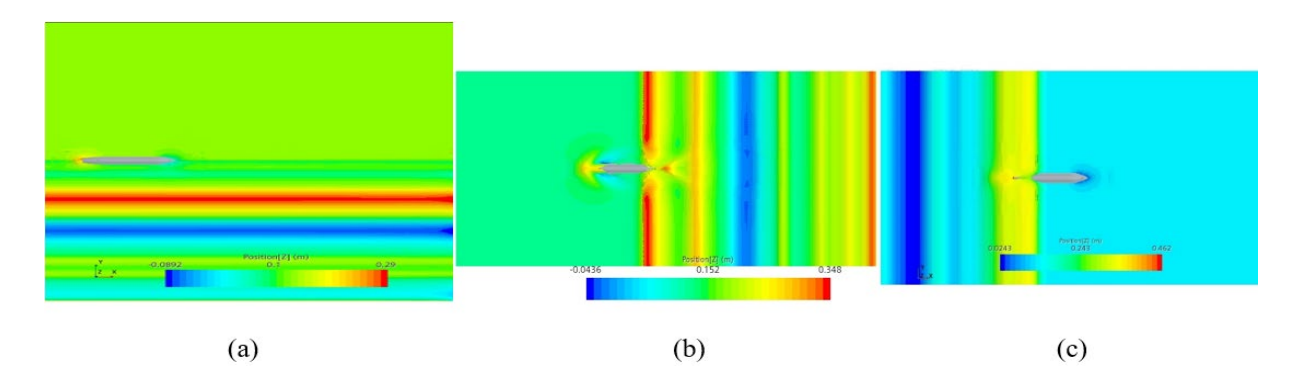


Figure 5. The initialized waves for different heading angles at D*=0.25: (a) 90°; (b) 0°; (c) 180°.

The volume fraction of water around the surface of the body is shown in Figure 5 (cases 10 and 15). The volume fraction of water is used to represent the state of the computational cell. A value of 1 indicates that the cell is filled with water, while a value of 0 indicates that the cell is filled with air. Figure 5 (a) illustrates the initialization of the following waves when the submarine is positioned on the free water surface ($D^*=0.25$). Additionally, Figure 5 (b) shows the head wave scenario, where the submarine is located below the free water surface ($D^*=1.1$).

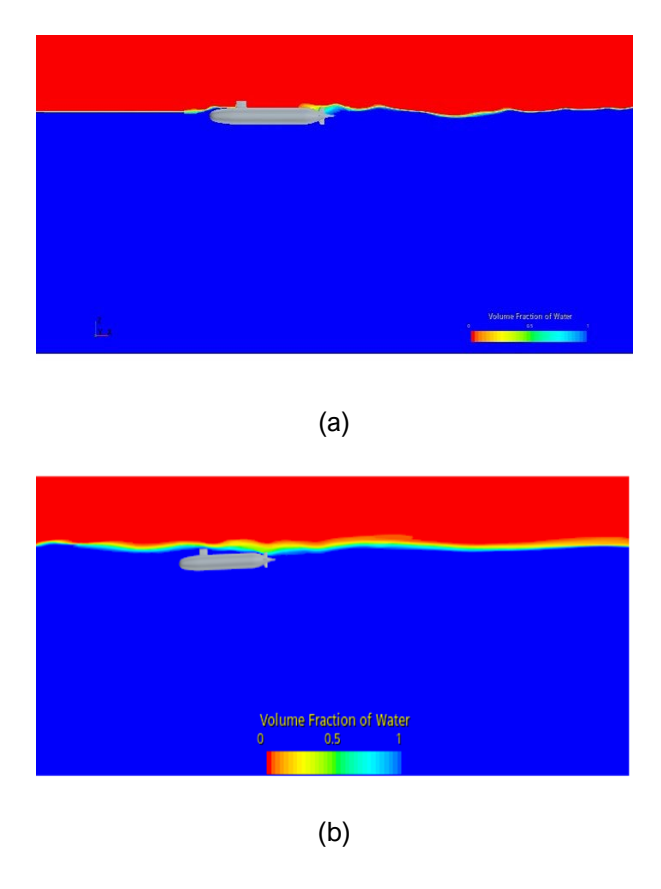


Figure 6. Volume fraction of water: (a) overview of initialized following sea with $D^*=0.25$ (case 10); (b) head sea with $D^*=1.1$ at t=95 (s) (case 15).

3. VERIFICATION AND VALIDATION PROCEDURE

3.1 Grid independence study

A non-uniform structured grid has been generated in the computational domain using several meshing methods to discretize the space. In this paper, the trimmer mesh and prism layer mesh methods were employed (Seo et al., 2010). The trimmed cells, using a hexahedral mesh with minimal cell skewness, create a high-quality grid that is suitable for complex simulations such as free-surface interactions. Therefore, the entire computational domain, except near the submarine hull, is discretized using a trimmer mesh. If wave generation is predictable, local filtering can be applied. Near the submarine hull, the solution lies within the boundary layer region. In this region, 9 layers of orthogonal prismatic cells are employed due to the high velocity gradient. These layers are generated using the trimmed mesh and the prism layer mesher. The computational grid consists primarily of hexahedral meshes, with a smaller number of polyhedral meshes close to the submarine model.

Regarding grid production, the ITTC (2011) recommends having at least 40 cells per length for regular waves, at least 20 cells for the shortest wavelength in irregular waves, and fewer than 10 cells per height for both regular and irregular waves. Additionally, CD-adapco (2020) suggests using 16 to 32 cells per wave height and 80 to 160 cells per wavelength for gridding the free surface. The number of cells used in this simulation exceeds the recommended values. For the free surface of the water, using fixed mesh dimensions in the y and x orientations improves the stability of the simulation (Romanowski et al., 2019). Figure 6 shows the grid in the computational domain and around the submarine. As shown in Figure 6, the grid density is higher at the

interface between the two fluids and near the submarine body. The boundary layer mesh elements are extruded from the AUV surfaces to improve computational grid quality and ensure sufficient accuracy in representing the boundary layer flow.

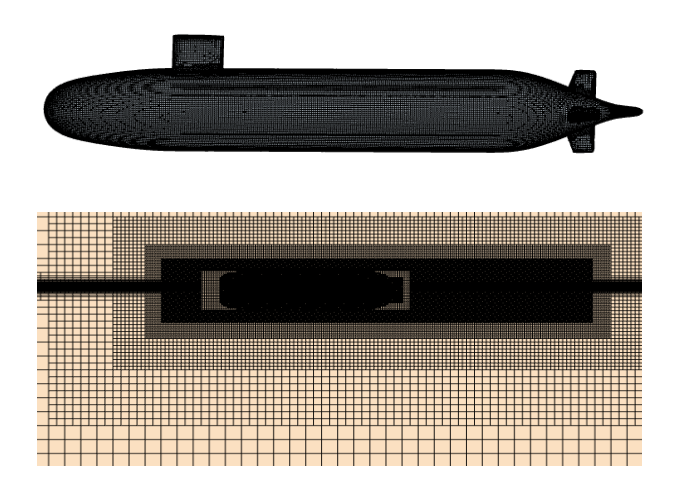


Figure 7. The grid structure of the computational domain.

Overset meshes are employed to discretize a computational domain using several different meshes that overlap arbitrarily. This approach is particularly beneficial for problems involving large motions, such as optimization research. The overset mesh method is adopted in this study to simulate submarine motion in waves (Huang et al., 2021). Figure 7 illustrates how the overset block moves with the submarine body while maintaining the mesh quality of the background block. Interpolation ensures the overset mesh aligns seamlessly with the background block.

The computational domain consists of five million cells, with 3.5 million cells in the background area and 1.5 million cells in the overset area. The dimensions of the overset region are $5.5 \times 1.4 \times 1$ meters. This setup ensures precise representation of the submarine's motion and interaction with the surrounding flow.

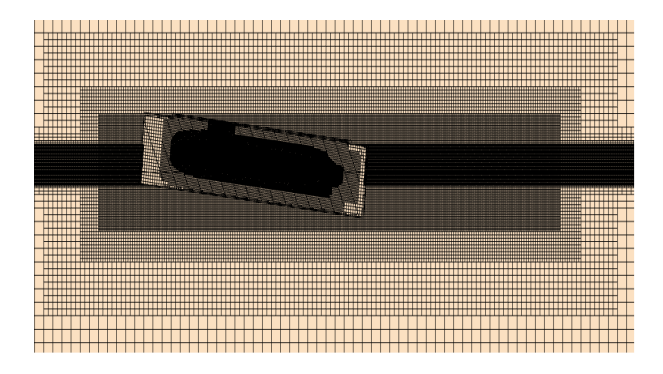


Figure 8. The overset block motion in the background block.

An appropriate time step is essential for performing transient numerical simulations to ensure accurate solutions while minimizing computational time. The ITTC (2011) recommends using at least 60 time steps within the shortest encountered wave period for irregular waves. The grid independence study, illustrated in Table 3, evaluates three different meshes. This study was conducted for Case 15, using a constant refinement factor (r_G) to achieve uniform mesh refinement in all directions (Amiri et al., 2018). The refinement factor ensures

proportional changes in cell sizes across sequential grids. However, due to the non-uniform nature of the grid, the ratio of cell numbers between consecutive grids does not strictly adhere to r_G .

Grid	I	II	III
Grids number (million)	3.3	4.8	7
Pitch (Degree)	0.1583	0.1634	0.1632
Heave (m)	0.0058	0.0061	0.0062
Roll (Degree)	0.1175	0.1201	0.1204

Table 4. Grid independence study.

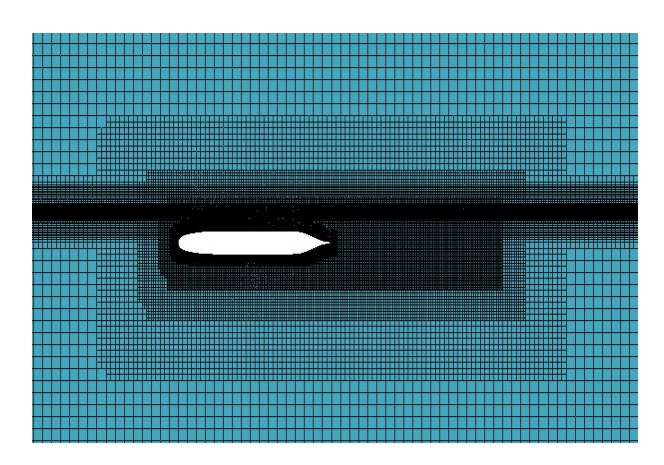
3.2 Validation

For the validation, Wilson-Haffenden et al. (2009) results have been used. Wilson-Haffenden et al. (2009) studied the effects of depth and Froud number on the drag coefficient of Suboff. This experiment research has been used to validate the results of many researchers (Amiri et al., 2018; Ling et al., 2022). Also, the drag coefficient is calculated from the following equation, where ρ is the water density, R denotes the total drag, C_T denotes the drag coefficient, S denotes the surface wetted area of submarine, and V denotes the speed of the submarine:

$$C_T = \frac{R}{\frac{1}{2}\rho SV^2} \tag{9}$$

Validation of the numerical results of the drag coefficient has been compared with the results of Wilson-Haffenden et al. (2009) experiment research. This experiment research has been used to validate the results of many researchers (Amiri et al., 2018; Ling et al., 2022). The validation in this paper is done at constant depth $(D^*=1.3)$ and different Froude numbers (0.13, 0.28, 0.36, 0.64).

High-quality unstructured trimmed meshes were generated in the computational domain for CFD simulations, as demonstrated in Figure 8 (Seo et al. (2010)). As shown in Figure 8 the grid density is significantly higher near the AUV and the water's free surface to capture critical interactions accurately. The computational domain contains approximately 2.8 million cells.



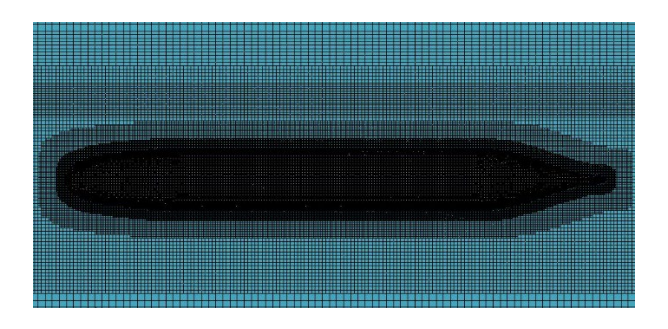


Figure 9. Grid computational domain in the validation.

To reduce computational time while maintaining accuracy, half of the computational domain was simulated by taking advantage of the symmetry in the geometry and flow physics. The symmetry boundary condition was applied along the plane of symmetry, enabling efficient calculations without compromising the quality of the results. (Jiao & Huang, 2020; Shivachev et al., 2020). Figure 9 shows a good agreement between the simulation results with the results of Wilson-Haffenden et al. (2009) and Shariati and Mousavizadegan (2017).

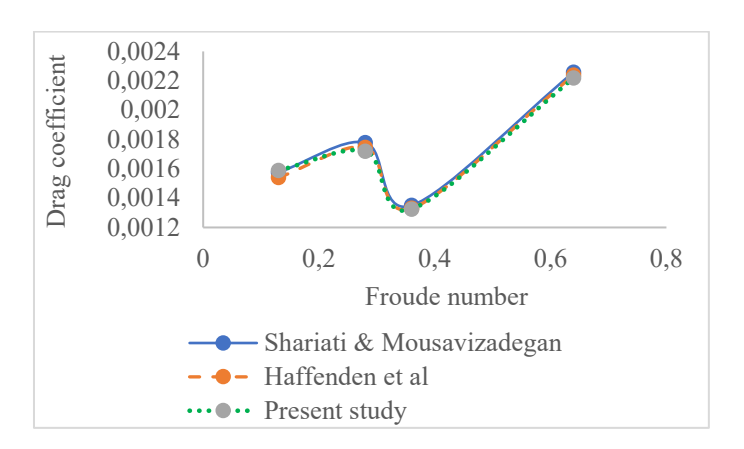


Figure 10. Comparison of the present results with Wilson-Haffenden et al. (2009) and Shariati and Mousavizadegan (2017).

Figure 10 illustrates the comparison of changes in the elevation of the free water surface caused by the motion of the submarine near the water surface with the results from Shariati and Mousavizadegan (2017). For this simulation case, the dimensionless depth is 1.3, and the Froude number is 0.55.

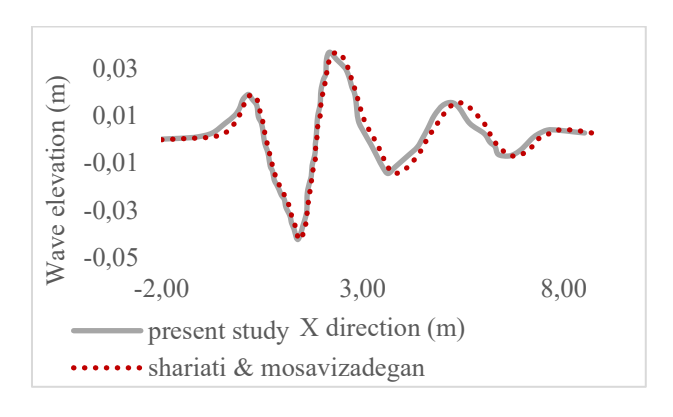


Figure 11. Comparison wave elevation.

3.3 Uncertainty analysis

Uncertainty analysis affiliated with temporal and spatial discretization requires the convergence ratio (R_G) computation from the results. R_G is defined as follows:

$$\begin{split} R_G &= \frac{\varepsilon_{G_{32}}}{\varepsilon_{G_{21}}} \\ \varepsilon_{G_{21}} &= \emptyset_{II} - \emptyset_I \\ \varepsilon_{G_{32}} &= \emptyset_{III} - \emptyset_{II} \end{split} \tag{10}$$

where \emptyset is the obtained value of the simulation in each of the grids. According to the above relationship, four states are possible (Stern et al., 2006). These simulation states are listed in Table 4.

R_G	Result
$1 > R_G > 0$	Asymptotic convergence
$0 > R_G > -1$	oscillatory convergence
$1 < R_G$	Asymptotic divergence
$-1 > R_G$	Oscillatory divergence
	$1 > R_G > 0$ $0 > R_G > -1$ $1 < R_G$

Table 5. The range of convergence

Divergence occurs in the third and fourth states and uncertainty can be checked only in the first and second states. In Table 5 lists the convergence ratios of HPR motions.

motion		Grid				
	fine	medium	coarse	R_G		
heave (m)	0.115	0.1166	0.1167	0.0934		
pitch	4.6182	4.4033	4.489	-0.3986		
roll	0.1766	0.1841	0.1851	0.1355		
roll	0.1766	0.1841	0.1851	0.13		

Table 6. Convergence ratios of HPR motions.

The R_G values indicate that the heave and roll motions exhibit asymptotic convergence, characterized by $0 < R_G < 1$. Meanwhile, the pitch motion demonstrates oscillatory convergence behavior, characterized by

 $-1 < R_G < 0$. The Grid Convergence Index (*GCI*) measures the discrepancy between the exact solution and the obtained numerical result. In the second stage, where oscillatory convergence occurs, the *GCI* is determined using equation (11).

$$GCI = \frac{1}{2} |\emptyset_U - \emptyset_L| * 100\%$$
 (11)

Where ϕ_L and ϕ_U are the minimum and maximum results of the convergence study, respectively. Table 6 shows the calculation of the convergence index for the pitch motion.

Motion	ø _U (degree)	$\emptyset_L(degree)$	%GCI
Pitch	4.4618	4.4033	2.923

Table 7. GCI for pitch motion.

In the first state, where there is uniform grid convergence, the results fall within the asymptotic range. In this scenario, the method proposed by Roache (1997) is applied to calculate the *GCI*. The refinement factor (r_G) is kept constant across the grids and is determined using the following equation, where Δx_G represents the cell size for each grid:

$$r_G = \frac{\Delta x_{GI}}{\Delta x_{GII}} = \frac{\Delta x_{GII}}{\Delta x_{GIII}} \tag{12}$$

 P_G is the discretization order which can be obtained as below:

$$P_G = \frac{\ln\left(\frac{1}{R_G}\right)}{\ln r_G} \tag{13}$$

It is important to note that the theoretical value of the discretization order can be 2. If $P_G>2$, high convergence of the discretization order is observed. However, such high convergence is often unreliable and may be a result of factors like the nonlinearity of the problem, turbulence modeling, and the quality of the mesh. In these cases, P_G should be replaced with the theoretical value of 2 when calculating the GCI (Eça and Hoekstra, 2009). The following equations are used to assess grid uncertainty, where F_S represents the safety factor.

$$e_{21} = \left| \frac{\emptyset_2 - \emptyset_1}{\emptyset_1} \right| \times \%100$$

$$GCI_{21} = F_S \left| \frac{e_{21}}{(r_{21}^{P_G} - 1)} \right| \tag{14}$$

The term e_{21} represents the relative error between grid 2 and grid 1, while e_{32} refers to the relative error calculated between grid 3 and grid 2. Since e is obtained in terms of percentage, the value of GCI will also be calculated in terms of percentage. It is suggested to the convergence study of three sequential grids, $F_S = 1.25$. The Table 7 shows the calculated values of P_G and GCI.

Va	riables	$F_{\mathcal{S}}$	R_G	r_G	P_G	% <i>e</i> ₂₁	%GCI _{21(GRoache)}	%e ₃₂	%GCI _{32(GRoache)}
motic	n heave	1.25	0.0934	1.2	13.6675	1.3912	3.9524	0.1260	0.3581

roll 1.25 0.1355 1.2 11.4903 4.2579 12.0965 0.5534 1.5	
--------------------------------------------------------	--

Table 8. Calculated grid uncertainty of the results of heave and roll motion

Finally, due to the negligible difference in the results between the medium and fine grids, simulations in this study were carried out using the medium grid. The number of cells in this grid is approximately 4.5 million for simulating head and following waves, and about 6 million for beam waves.

In the simulations conducted in this paper, the Jonswap wave spectrum with N = 50 components was used to generate irregular waves. The theoretical energy of the Jonswap wave spectrum is obtained as follows:

$$S_{J}(\omega) = A_{\gamma} S_{PM}(\omega) \gamma^{exp \left(-0.5 \left(\frac{\omega - \omega_{p}}{\sigma \omega_{p}}\right)^{2}\right)}$$
(15)

 $S_f(\omega)$ represents the JONSWAP spectrum as a function of angular frequency ω , while $S_{PM}(\omega)$ is the base Pierson-Moskowitz spectrum. The parameter A_γ is a normalization factor that ensures the proper energy distribution across the spectrum. The parameter γ is the peak enhancement factor, which controls the sharpness of the spectral peak, and ω_p denotes the peak angular frequency, indicating where the maximum energy is concentrated in the spectrum. Lastly, σ is the standard deviation.

Irregular waves were generated by superimposing linear wave components derived from the JONSWAP spectrum. To validate the generated waves, the free surface elevation was recorded over time at specific points in the computational domain. The time-series data was then exported and analyzed in MATLAB. Using MATLAB's Fast Fourier Transform (FFT) function, the signal was converted from the time domain to the frequency domain to compute the energy. The resulting spectrum was compared to the theoretical JONSWAP spectrum to ensure the accuracy of the generated waves. Figure 11 shows the theoretical and numerical wave energy spectrum. The numerical results for wave spectrum energy show good agreement with the theoretical predictions. In this case H_S =0.465(m) and T_p =2.455(s).

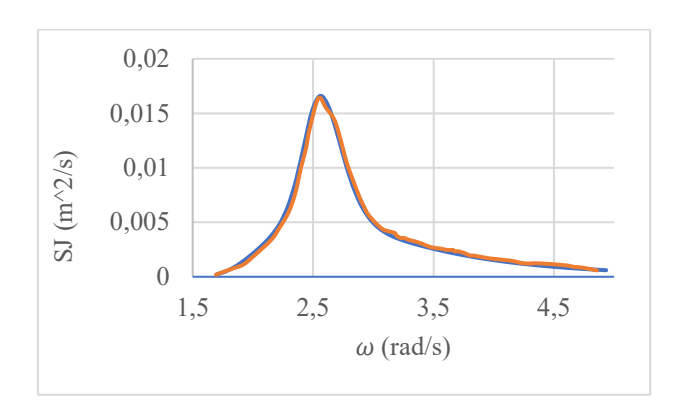


Figure 12. Comparison of the numerical and theoretical wave energy spectrum.

4. RESULTS

In this section, the hydrodynamic response of the submarine in irregular waves and calm water is presented and discussed. The results, obtained using the unsteady RANS method, are shown in polar plots for the RMS and maximum amplitudes of heave, pitch, and roll motions. Additionally, the response amplitude of motions and resistance are presented in the frequency domain.

In this section, the hydrodynamic response of the submarine in both irregular waves and calm water is presented and discussed. The results are primarily obtained using the unsteady RANS method, which involves more comprehensive simulations capable of capturing nonlinear and viscous effects. The motion responses, including RMS and maximum amplitudes of heave, pitch, and roll, are shown in polar plots, while frequency-domain analyses of motion amplitudes and resistance are also provided. Additionally, to highlight the differences between the CFD-based approach and simplified potential flow-based methods, a comparison with results from Maxsurf Motion using strip theory and panel method is included.

4.1 CFD and BEM Comparison

The selection of CFD based on the URANS approach in this study is motivated by its well-established capability to resolve nonlinear, viscous, and turbulent flow phenomena, particularly in near-surface operations where complex interactions between the submarine hull, the free surface, and incident waves are present. Prior studies have shown that URANS-based methods generally yield better agreement with experimental data compared to potential flow solvers, especially in predicting added resistance and roll motions where nonlinear and viscous effects are significant (Huang et al., 2021, Shivachev et al., 2020, Sigmund and El Moctar, 2018).

Potential flow methods, such as those implemented in boundary element method (BEM) tools, offer computationally efficient and time-saving solutions for linear wave-body interactions. However, they are inherently limited in capturing critical physical phenomena such as flow separation, vortex shedding, and nonlinear free-surface effects, which strongly influence submarine hydrodynamics near the surface. A comparative analysis was conducted between the URANS-based CFD results and those obtained from Maxsurf Motion using strip theory and the panel method, both of which are potential flow-based approaches. The comparison was carried out under irregular wave conditions with a significant wave height of 0.08 m, a peak period of 1.75 s, a non-dimensional water depth of 0.25, and a Froude number of 0.3146. While strip theory is applicable in the presence of a free surface and the panel method is suited for near-zero forward speed, both were included despite their respective limitations. As presented in Table 8, the results demonstrate that heave and pitch motions predicted by the potential flow methods align more closely with the CFD results. In contrast, roll motion exhibits greater discrepancies, suggesting a stronger dependence on viscous and turbulent effects that are not captured by potential flow formulations.

CFD	Strip theory	Panel method
0.007374	0.0108	0.0151
0.883434	0.6701	1.3851
0.125063	0.4451	0.5087
	0.007374	0.007374 0.0108 0.883434 0.6701

Table 9. RMS Motion Comparison Between Methods.

4.2 Calm Water Results

Table 8. shows the RMS and maximum amplitude of submarine motions in both surface mode ($D^*=0.25$) and submerged mode ($D^*=1.1$) under calm water conditions. The results indicate that the amplitude of pitch and

heave motions is greater in the submerged mode compared to the surface mode, while the amplitude of roll motions increases in the presence of the free surface.

Case number	heave rms (m)	heave max (m)	pitch rms (°)	pitch max (°)	roll rms (°)	roll max (°)
case13-flat -1.1d	0.1828	0.1344	2.5946	3.75	0.1601	0.0296
case2-flat-0.25d	0.0019	0.0046	0.9606	1.1021	0.8964	0.5060

Table 10. Amplitude of submarine motions in the surface mode and submerged mode at calm water.

The total resistance (R_T) of a submarine is obtained as follows:

$$R_T = R_R + R_F \tag{16}$$

Where R_F denotes the frictional resistance between the fluid and the hull surface, and R_R represents the residual resistance. Statistical values such as the mean and standard deviation (SD) of the results are provided below:

$$\bar{X} = \frac{\sum_{i=1}^{N} X_i}{N} \tag{17}$$

$$SD = \sqrt{(\frac{\sum_{i=1}^{N}(X_i - \bar{X})^2}{N})}$$

Figure 12 compares the submarine's drag force in calm sea conditions with and without HPR motions. The submarine is positioned at two different water depths, referred to as the submerged mode ($D^*=1.1$) and the surface mode ($D^*=0.25$). The results indicate that allowing the submarine freedom of motion significantly increases the residual resistance compared to the submarine without HPR motions, while the frictional resistance remains nearly constant. The pitch motion alters the flow's angle of attack, thereby affecting the residual resistance. Since the amplitude of the pitch motion in the submerged mode ($D^*=1.1$) is greater than in the surface mode ($D^*=0.25$) as shown in Table 8, the increase in residual resistance is expected to be more pronounced in the submerged mode than in the surface mode. Additionally, the resistance in the surface mode is higher than in the submerged mode due to the greater effect of waves on the submarine's motion in the surface mode. The standard deviation (SD) value increases slightly with the freedom of motion of the submarine.

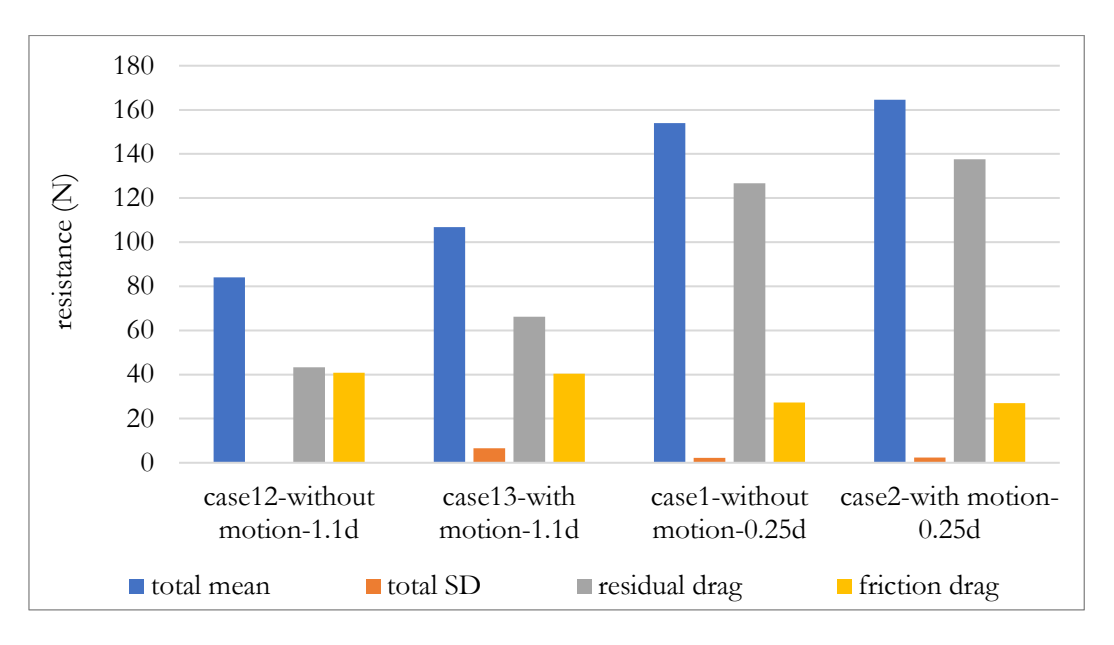


Figure 13. Submarine resistance force with and without HPR motions in calm water.

4.3 Irregular wave results

4.3.1 Heave motion

Figure 13 shows the calculated time series of submarine heave motions in surface mode.

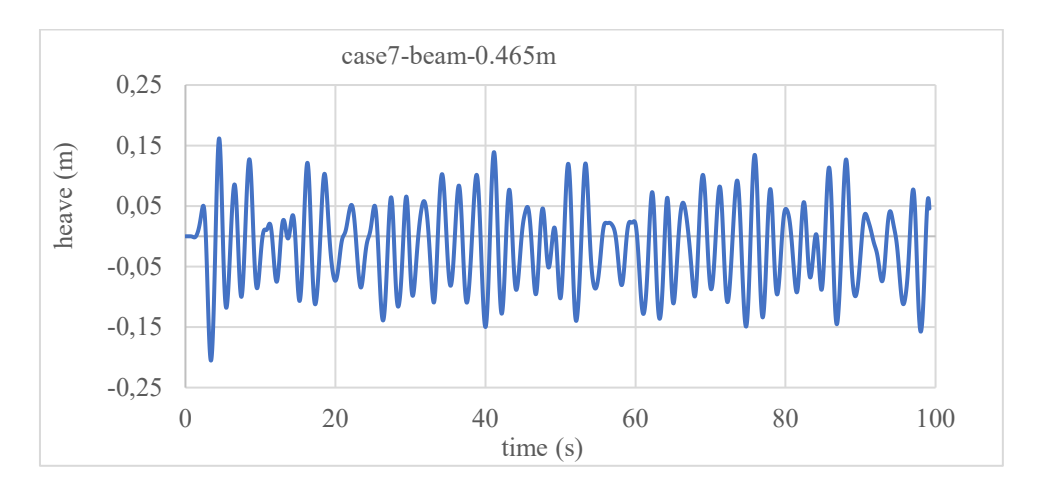
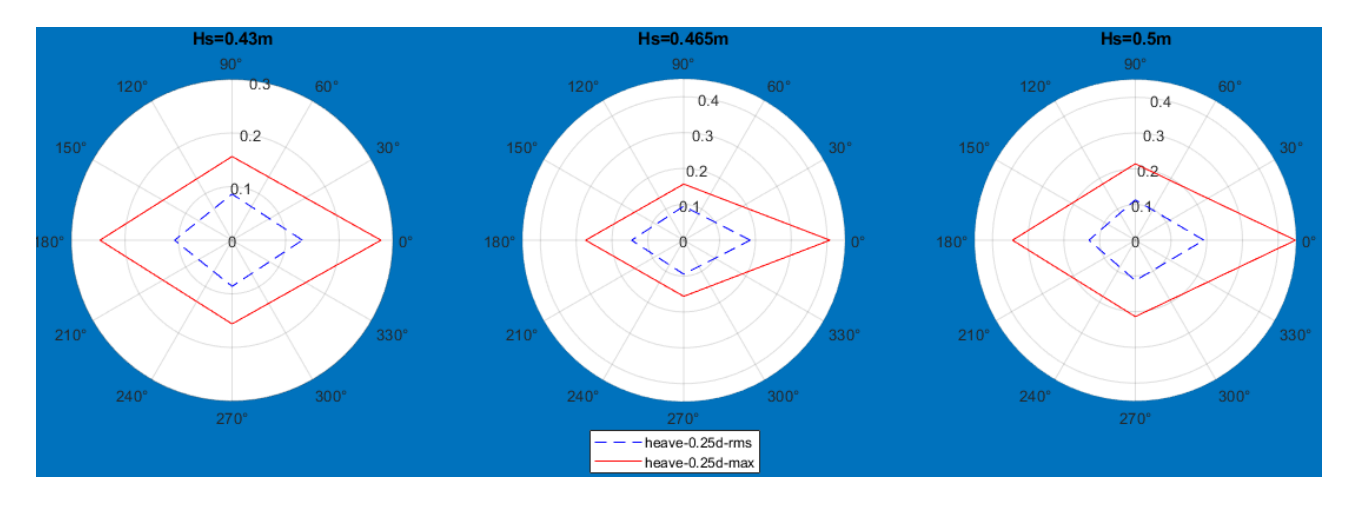


Figure 14. Time series of submarine heave motions for Case 7.

Figure 14 shows the polar coordinate system of the root mean square (RMS) and maximum response amplitude (MAX) of heave motion, based on time series results for submarine heave motion across all simulation cases. According to the results, in the surface mode, the maximum and minimum heave amplitudes occur in the following and beam waves, respectively. In the submerged mode, the largest and smallest heave responses are observed in the following and head waves, respectively. In both surface and submerged modes, as the significant wave height increases, the amplitude of heave motion increases in the following and head waves. In beam waves, the amplitude of heave motion shows only a slight change with increasing significant wave height. In the surface mode, the increase in heave motion amplitude with significant wave height is more pronounced than in the submerged mode.



(a)

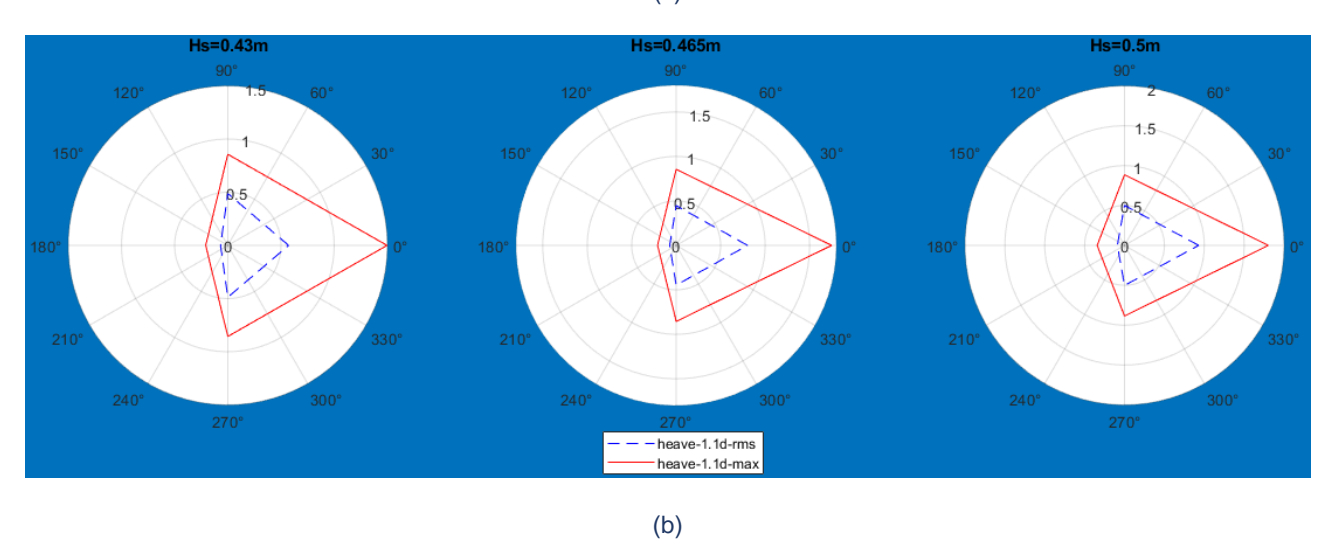


Figure 15. Polar plot of heave motion amplitude at different wave heading angles (a) 0.25d, (b) 1.1d.

The frequency domain results of heave motion are derived by using Fast Fourier Transformation (FFT) from time series results. This approach is applied to derive the frequency domain data. The encounter frequency can be also estimated as follows:

$$\omega_e = \omega \left(\frac{V \omega \cos \beta}{g} + 1 \right) \tag{18}$$

Where V is the submarine speed, ω is the frequency, β is the wave direction, g is the acceleration due to gravity, and ω_e is the encounter frequency.

Figure 15 presents the frequency-domain spectra of the submarine's heave motion in surface mode under various wave heading angles and significant wave heights. The heave motion response spectra of the submarine in surface mode, under various wave headings and significant wave heights (Hs), reveal clear trends. The spectral energy of heave motion is highest in following seas, indicating that waves approaching from behind generate stronger and more sustained heave responses. In comparison, the response energy is lower in head seas and reaches its minimum in beam seas, where the heave excitation is least pronounced. As the significant wave height increases, the overall spectral energy also increases, showing that higher sea states lead to stronger heave responses. Moreover, in following sea conditions, the peak of the heave response

spectrum shifts toward lower frequencies, suggesting that the dominant heave motion is influenced by slower wave components. These findings highlight the significant impact of both wave direction and wave height on the heave behavior of submarines operating near the free surface.

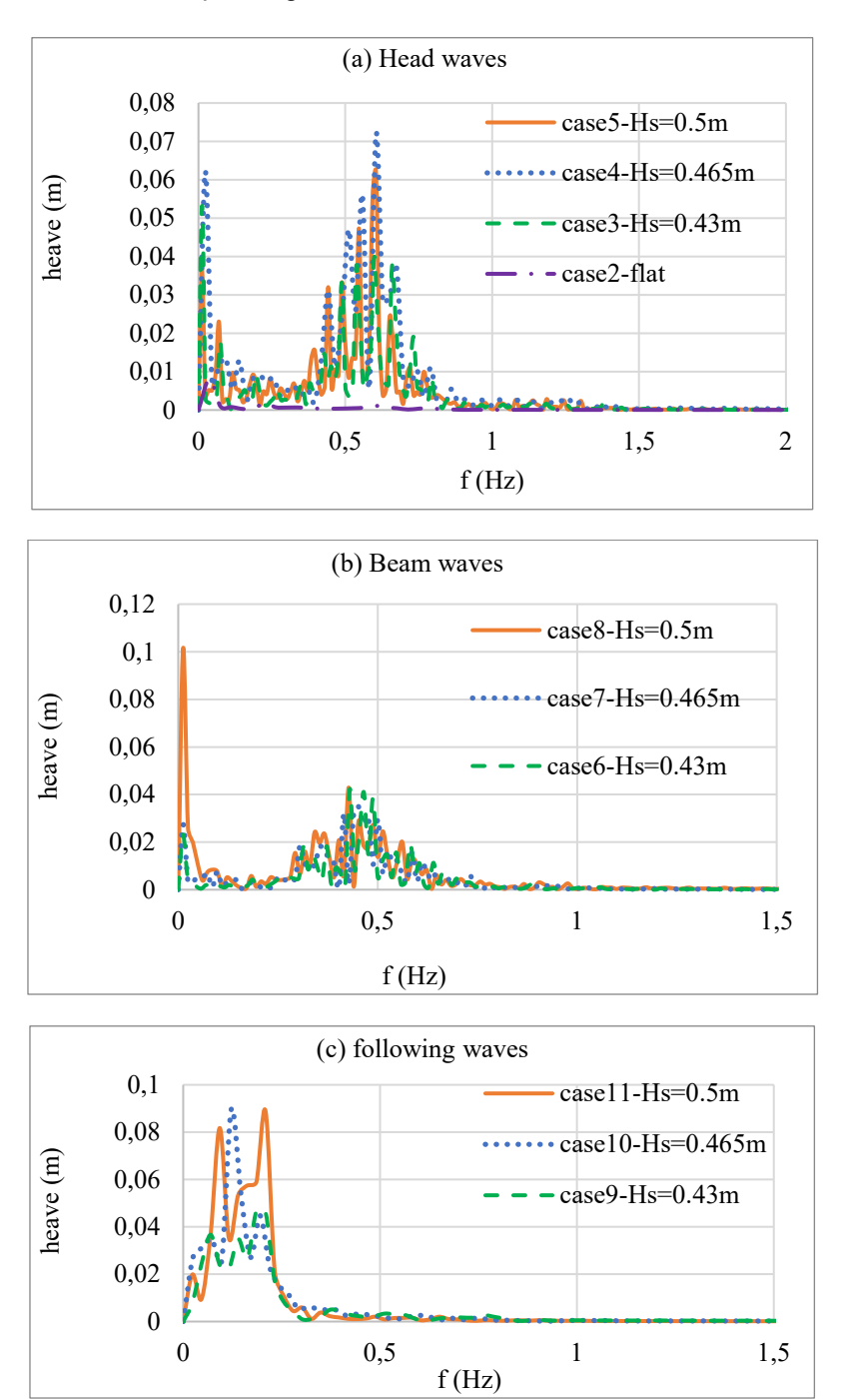
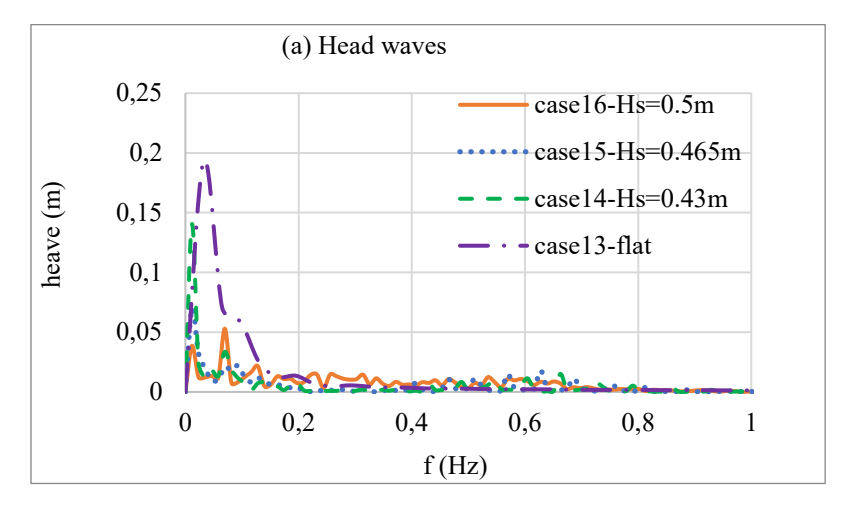
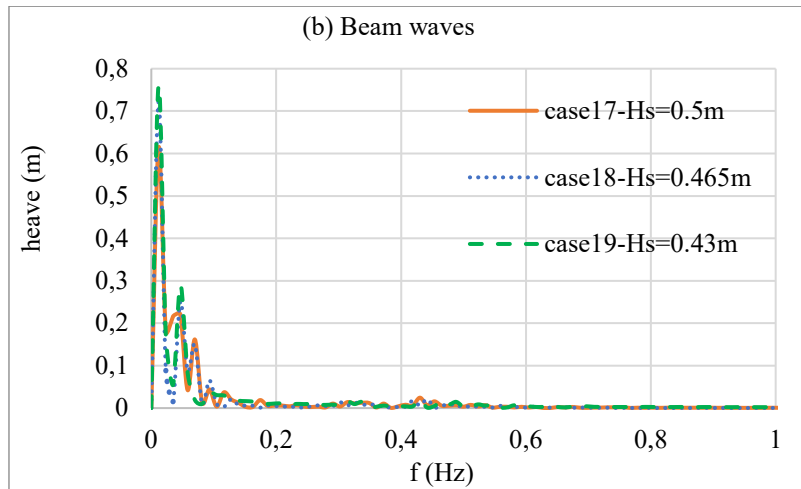


Figure 16. Submarine heave motion spectra versus wave frequency for different wave headings and significant wave heights (Hs) in surface mode: (a) Head waves, (b) Beam waves, (c) Following waves.

In comparison, Figure 16 illustrates the frequency-domain spectra of the submarine's heave motion in submerged mode, showing similar dependencies on wave heading angles and wave heights. In the surface mode, the heave motion spectrum is more influenced by the encounter frequency and less by the natural frequency of the submarine's motions. In the surface mode, when the submarine moves upward due to the

wave excitation force, the volume inside the submarine decreases, resulting in a reduction of the buoyancy force while the weight remains constant.





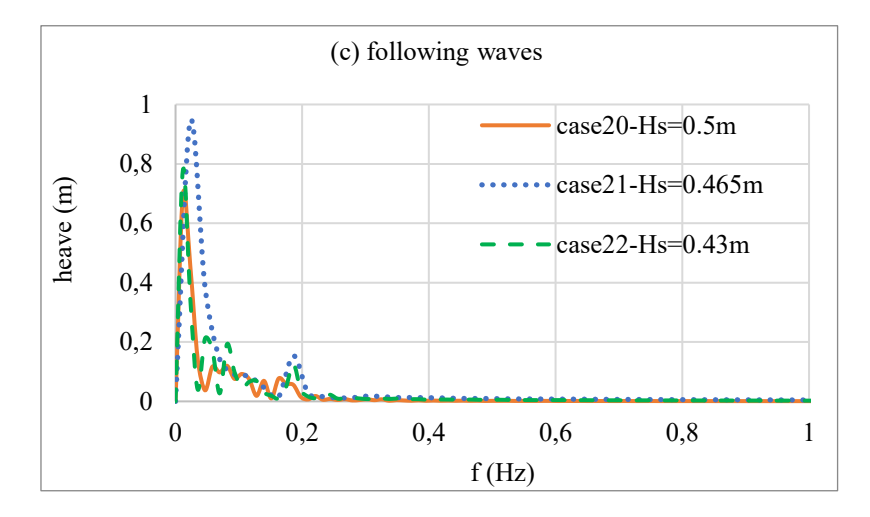


Figure 17. Submarine heave motion spectra versus wave frequency for different wave headings and significant wave heights (Hs) in submerged mode: (a) Head waves, (b) Beam waves, (c) Following waves.

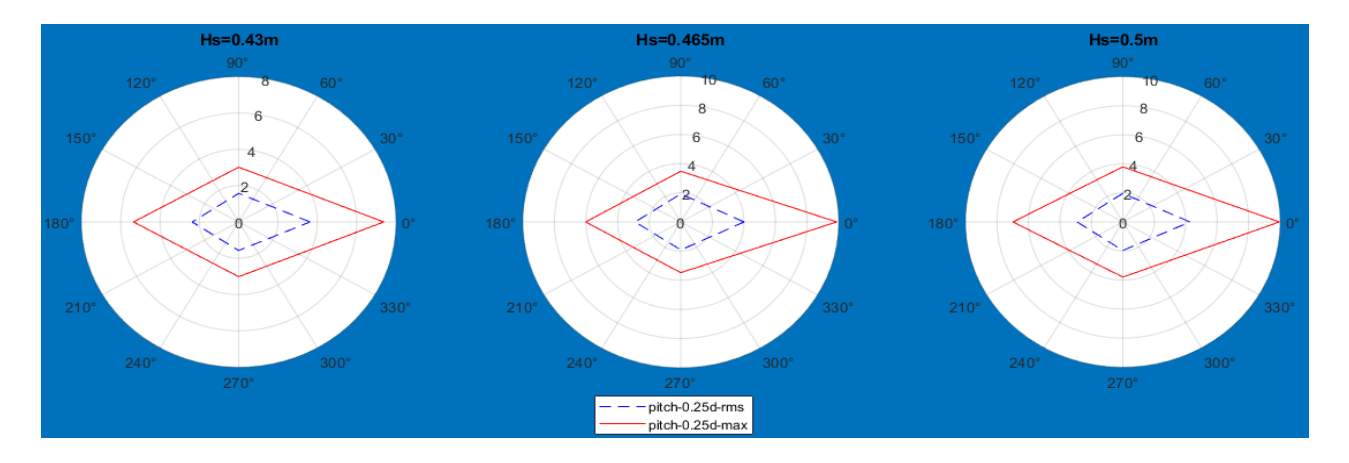
As a result, the submarine moves downward. Conversely, when the submarine moves downward due to wave excitation, the volume inside the submarine increases, leading to a rise in the buoyancy force, while

the weight stays constant, causing the submarine to move upward. In the submerged mode, since both the weight and buoyancy forces are constant, the heave motion changes solely due to the wave excitation force. As a result, the oscillation of heave motion in the surface mode is more pronounced than in the submerged mode.

4.3.2 Pitch motion

The root mean square (RMS) and maximum response amplitude of the pitch motion for all wave heading angles are shown in Figure 17, which derived from the time series data for submarine pitch motion. The results indicate that in the surface mode, the maximum and minimum pitch amplitudes occur in the following and beam waves, respectively. In the submerged mode, the largest pitch motion amplitude occurs in the following wave, while the lowest amplitude occurs in the head wave. In both surface and submerged modes, as the significant wave height increases, the amplitude of pitch motion increases for the following and head waves. In beam waves, however, the amplitude of pitch motion changes slightly with increasing significant wave height. Notably, the increase in pitch motion amplitude with significant wave height is more pronounced in the submerged mode than in the surface mode.

When the submarine is in submerged mode, the center of buoyancy serves as both the longitudinal and transversal metacenter. In the surface mode, the longitudinal rotation of the submarine alters the characteristics of the draft plate, which raises the height of the metacenter compared to the submerged state. As a result, the coefficient of the pitch restoring moment, which depends on the height of the longitudinal metacenter, increases in the submerged state. This explains why the amplitude of pitch motion in the submerged mode is greater than in the surface mode.



(a)

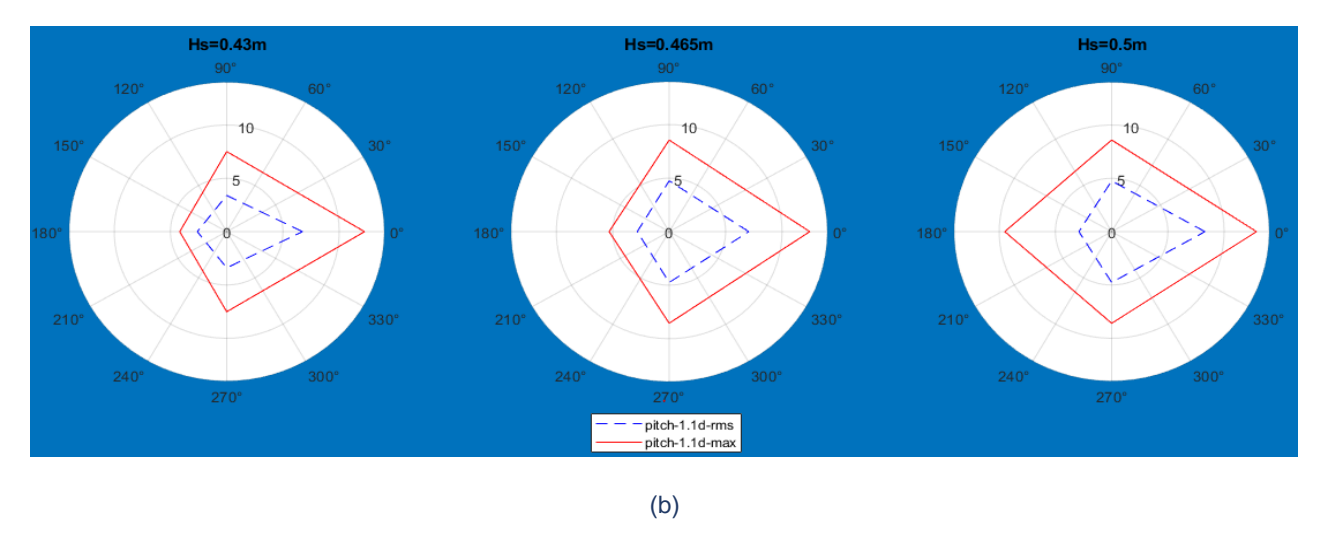
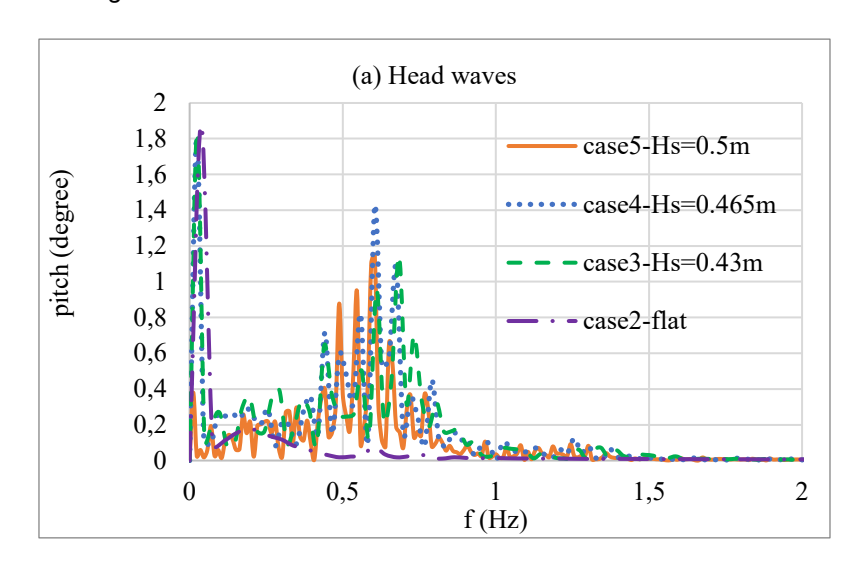


Figure 18. Pitch motion amplitude at different wave heading angles: (a) 0.25d; (b) 1.1d.

To obtain the pitch motion spectra in surface mode, the Fast Fourier Transform (FFT) method was applied to various wave heading angles and different wave heights, as shown in Figure 18. The results show that as the significant wave height increases, the overall spectral response of pitch motion also intensifies, indicating a greater energy transfer from the waves to the submarine's motion. Among the wave headings, the beam seas exhibit the lowest spectral response, while the head seas produce the highest response amplitudes, highlighting a stronger coupling between wave direction and pitch motion in head-on conditions. Moreover, the frequency at which the peak response occurs varies with wave heading. In following seas, the peak pitch response shifts toward lower frequencies due to the longer encounter periods, whereas in head seas, the peak occurs at higher frequencies, corresponding to the shorter and more frequent wave interactions. This variation underscores the directional sensitivity of pitch motion, which is more reactive to head wave energy and less excited in beam or following wave encounters.



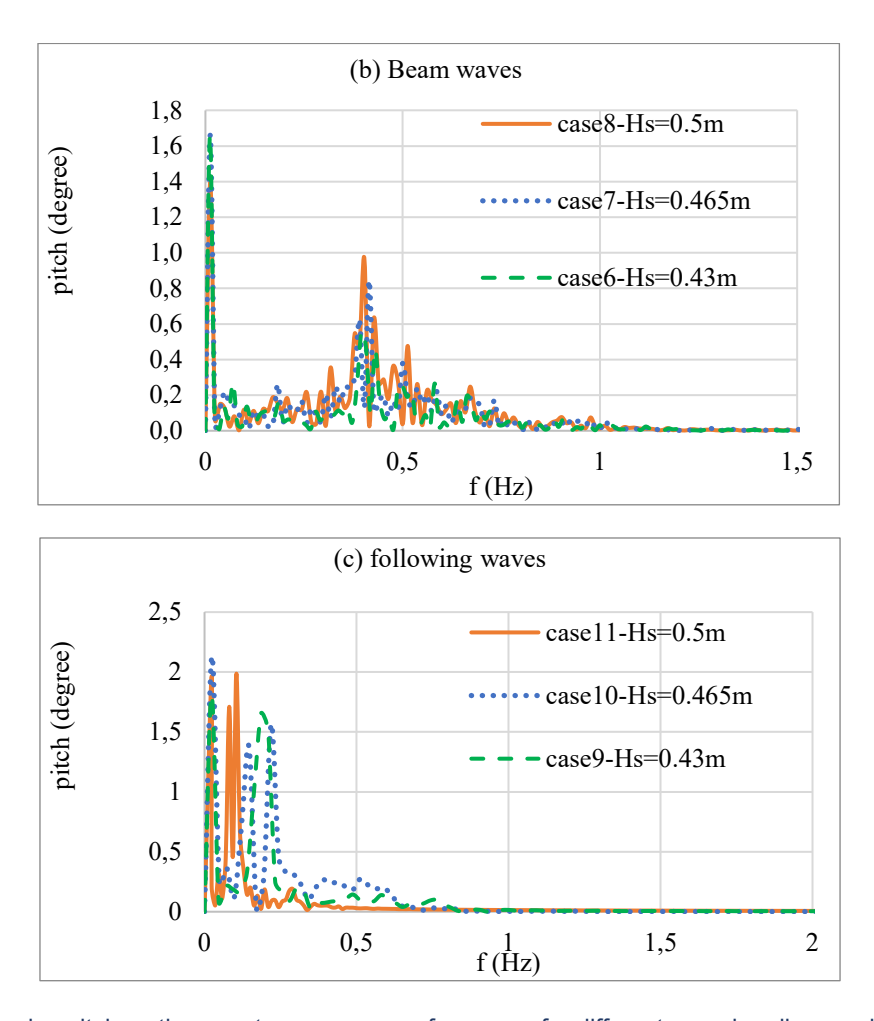


Figure 19. Submarine pitch motion spectra versus wave frequency for different wave headings and significant wave heights (Hs) in surface mode: (a) Head waves, (b) Beam waves, (c) Following waves.

Figure 19 presents the frequency-domain spectra of the submarine's pitch motion in submerged mode under various wave heading angles and significant wave heights. Compared to the surface mode, the overall response patterns remain similar, with a slight shift observed in the location of the spectral peaks. Specifically, in both beam and head seas, the peak spectral responses occur at lower frequencies than in the surface condition. In general, the surface mode shows a higher peak frequency for the pitch motion spectra than the submerged mode. For most simulation cases, the peak of the motion spectrum for shorter waves occurs at higher frequencies, suggesting that the responses are more influenced by the encounter frequency and less by the natural frequency of the submarine's motions. Notably, the peaks of both pitch and heave motion spectra occur at similar frequencies, and the maximum amplitude for these motions is observed at similar wave heading angles. This indicates that these motions are interdependent.

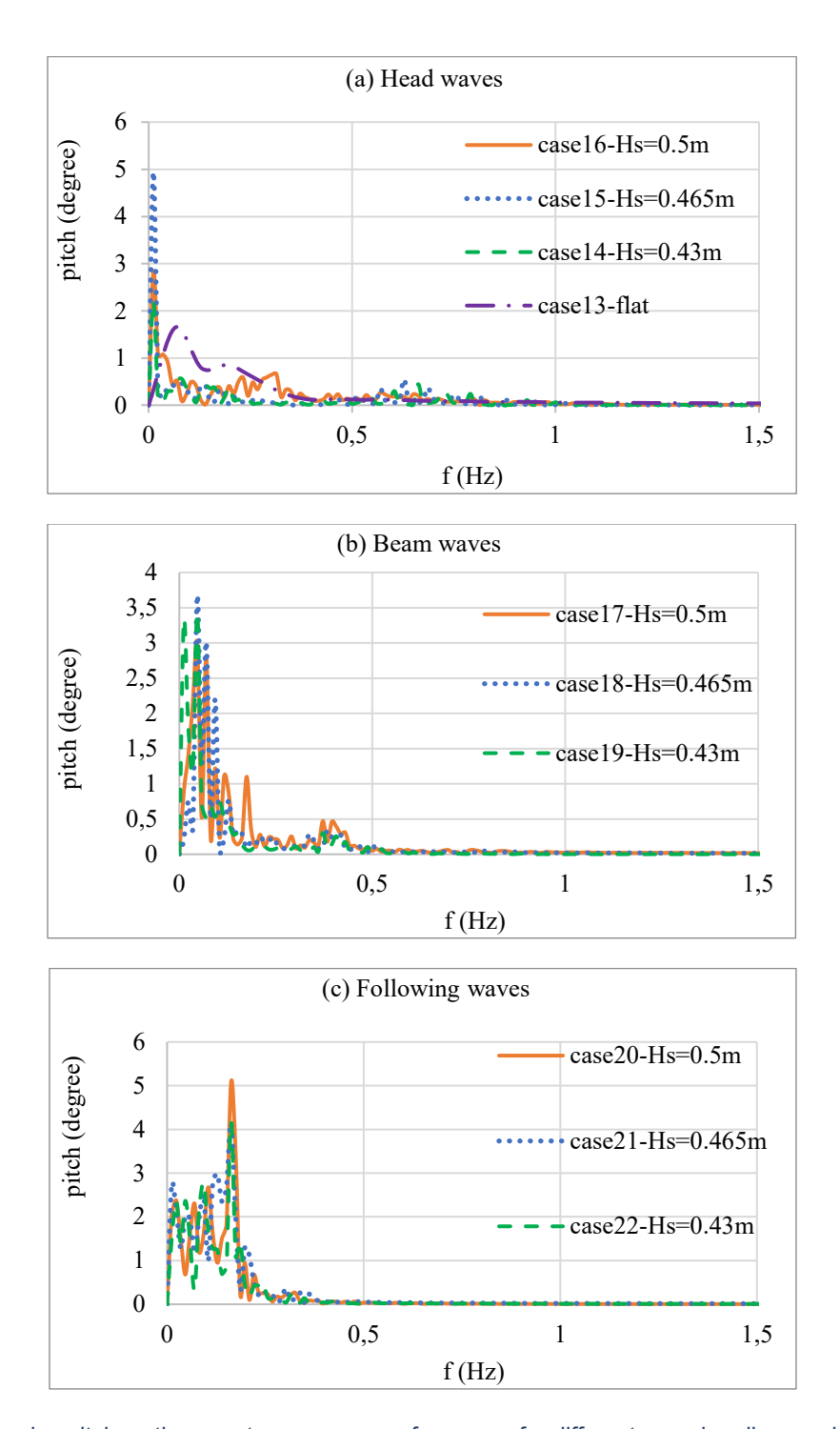


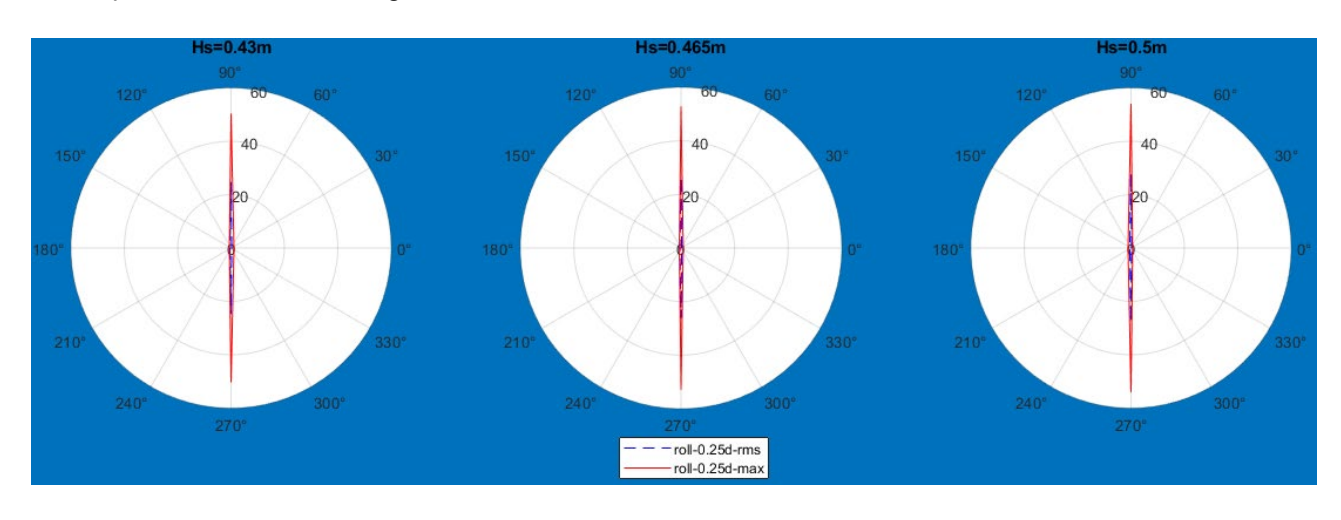
Figure 20. Submarine pitch motion spectra versus wave frequency for different wave headings and significant wave heights (Hs) in submerged mode: (a) Head waves, (b) Beam waves, (c) Following waves.

4.3.3 Roll motion

The root mean square and the maximum response amplitude, obtained from the time series data of the submarine's roll motion, are presented in Figure 18. The amplitude of roll motion is higher in the surface mode compared to the submerged mode. Additionally, for beam waves, the roll motion amplitude is greater than for other wave heading angles. Specifically, in the surface mode, the roll motion amplitude in beam waves

increases by 375% compared to the submerged mode. The amplitude of roll motion is also higher in head waves than in following waves. In both surface and submerged modes, as the significant wave height increases, the amplitude of roll motion increases.

For the submarine, the transverse metacenter remains unchanged in both surface and submerged modes, and the metacenter point does not shift with the submarine's transverse rotation. Consequently, the coefficient of the roll restoring moment, which is based on the length of the transverse metacenter, stays constant. Since the wave effects are more pronounced in the surface mode compared to the submerged mode, the amplitude of roll motion is greater in the surface mode.



(a)

Figure 21. Roll motion amplitude at different wave heading angles: (a) 0.25d; (b) 1.1d.

(b)

The derived frequency domain of submarine roll motions in surface mode various wave heading angles and significant wave heights (Hs) are shown in Figure 21. The results indicate that the lowest spectral response occurs in following seas, while the highest is observed in beam seas. This reflects the known sensitivity of roll motion to beam wave excitation. This indicates that, in beam waves where the maximum amplitude of the roll motion spectrum is observed, the responses are less dependent on the natural frequency of the submarine's motions. In head seas, the peak response appears at the lowest frequency among the three headings, whereas in beam seas, the peak occurs at the highest frequency. According to equation (18) as the wave period and

significant wave height increase, the encountered wave frequency decreases. Consequently, the responses can be considered to be related to the encountered frequency.

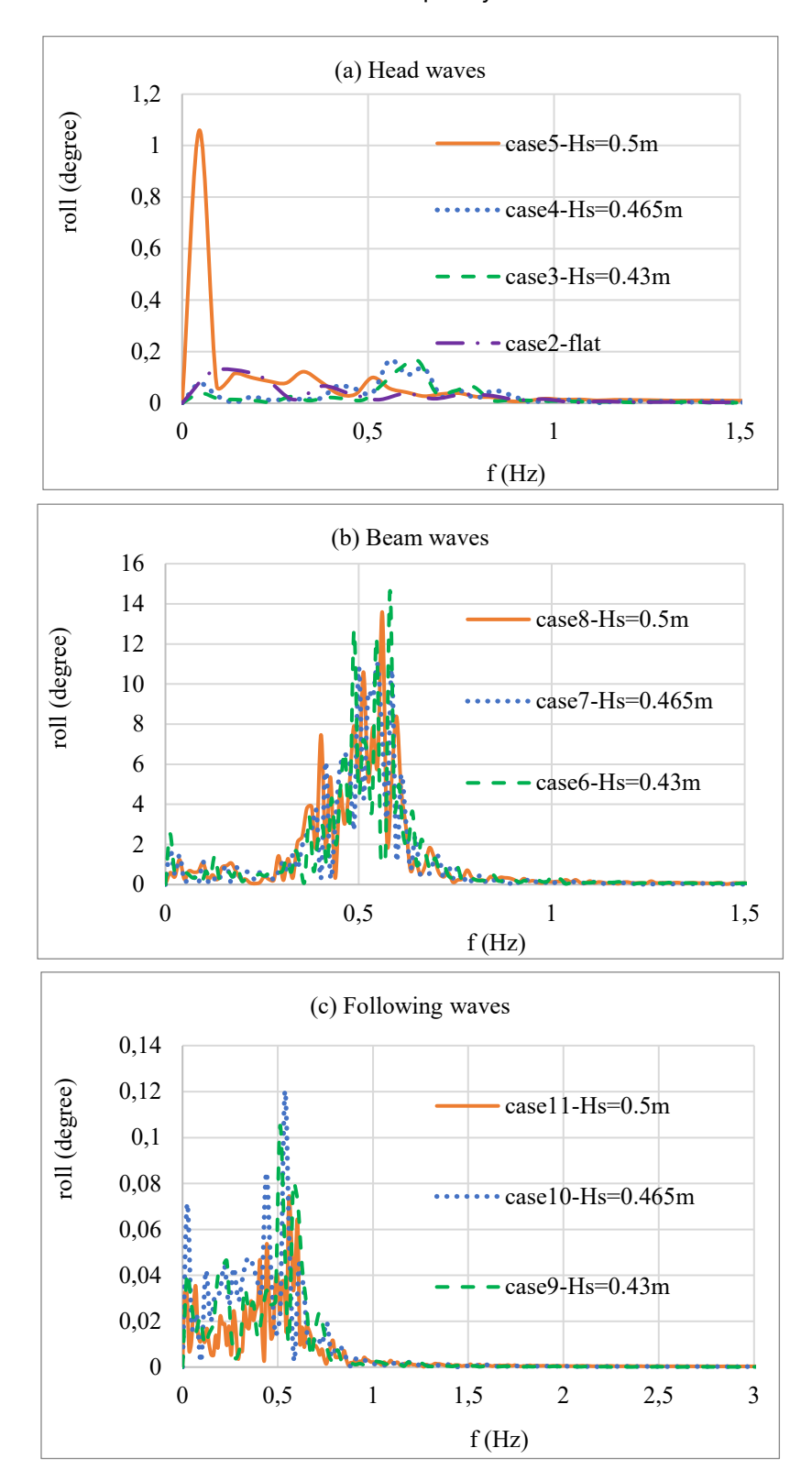
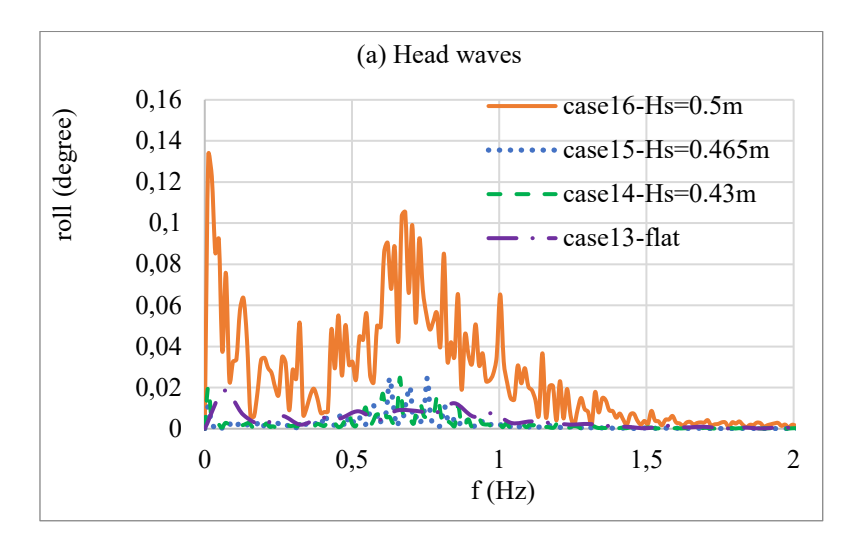
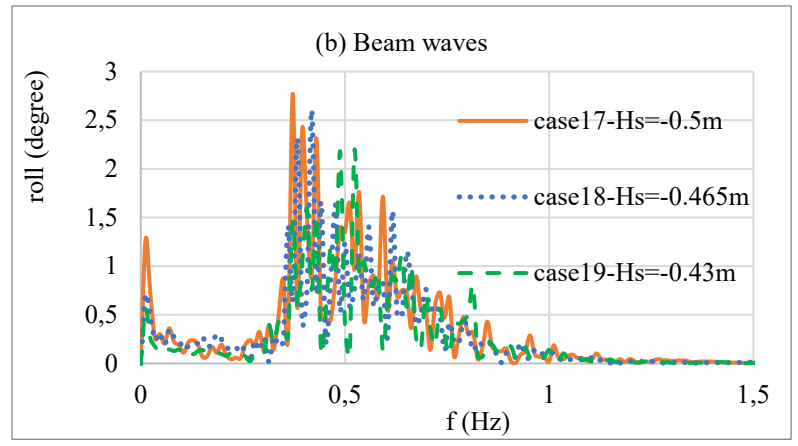


Figure 22. Submarine roll motion spectra versus wave frequency for different wave headings and significant wave heights (Hs) in surface mode: (a) Head waves, (b) Beam waves, (c) Following waves.

Moreover, as the significant wave height increases, the magnitude of the response spectrum increases across all headings. Additionally, the peak response shifts toward higher frequencies with greater wave heights, indicating that stronger waves induce more energetic and slightly faster oscillations.

Figure 22 presents the Fast Fourier Transformation of the roll motion amplitude for different heading angles and significant wave heights (Hs) in submerged mode. While the overall spectral distribution remains comparable to the surface case, a notable difference is observed in the location of the peak frequencies. In submerged conditions, the peak responses tend to occur at lower frequencies, highlighting the damping effect of depth. This frequency shift suggests that, similar to pitch motion, roll oscillations also become slightly slower when submerged. Aside from this frequency reduction, the general pattern and sensitivity to wave headings remain consistent with the surface case.





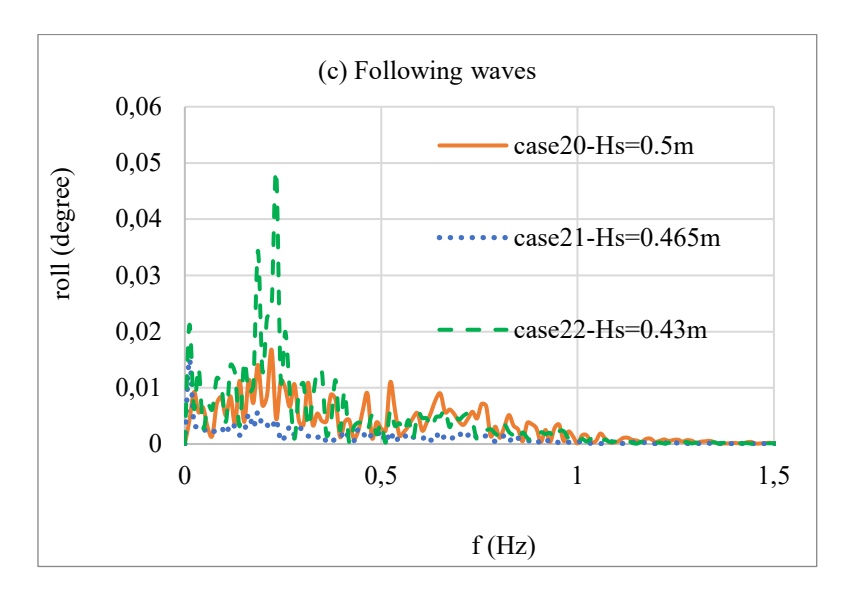
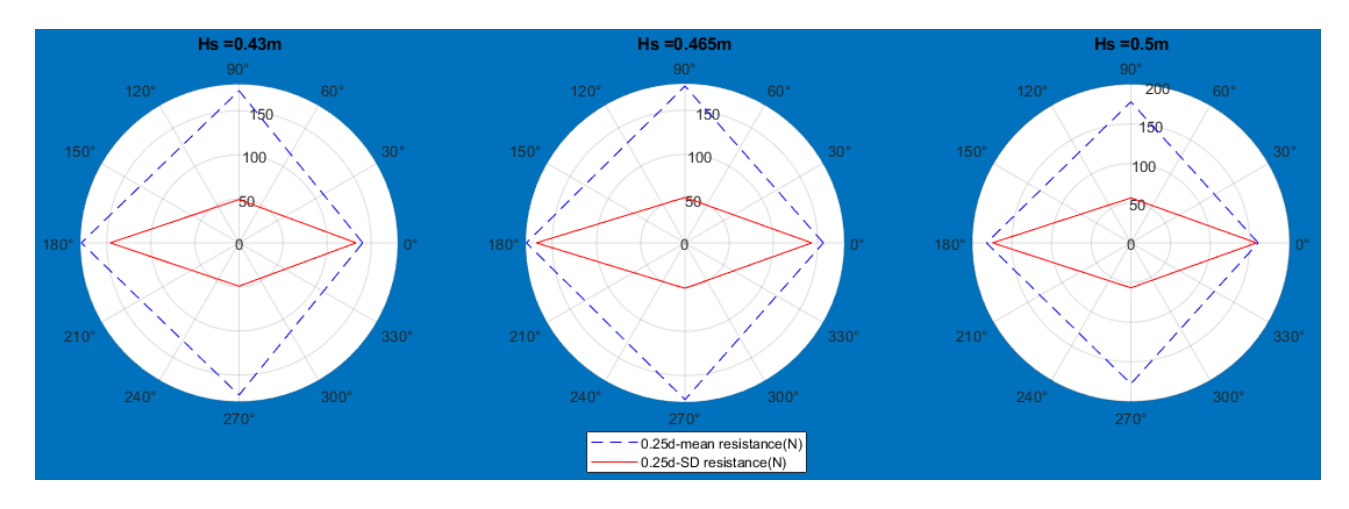


Figure 23. Submarine roll motion spectra versus wave frequency for different wave headings and significant wave heights (Hs) in submerged mode: (a) Head waves, (b) Beam waves, (c) Following waves.

4.3.4 Resistance calculation

The polar coordinate system of the mean (labeled as "mean") and the standard deviation (labeled as "SD") of the resistance force are shown in Figure 23, which presents the time-domain results for the submarine's resistance force across all simulation cases. As observed from the results, in both surface and submerged modes, the largest mean resistance force occurs in the head wave, while the lowest mean resistance force occurs in the following wave. In both modes, the highest standard deviation (SD) is observed in the head waves, and the lowest SD occurs in the beam waves. The increase in the standard deviation of the resistance force with increasing wave significant height is greater than the increase in the mean value of the resistance force. The mean drag value in the surface mode is higher than in the submerged mode, while the standard deviation remains relatively unchanged between the surface and submerged modes.



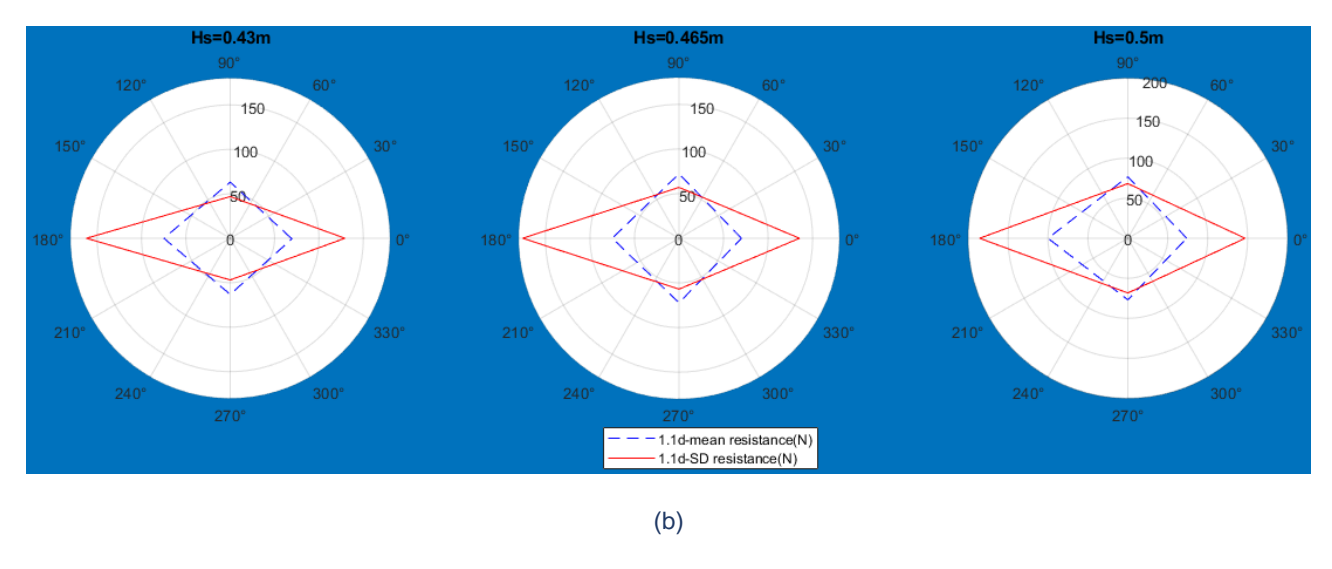


Figure 24. Resistance force at different wave heading angles: (a) 0.25d; (b) 1.1d.

Figure 24 shows the Fast Fourier Transform of the resistance force, presenting the frequency-domain data for various wave heading angles and significant wave heights in surface mode. In head waves, the peak response appears at the highest frequency among the examined cases, indicating more frequent oscillatory loading due to direct wave impacts. In contrast, the beam wave condition shows a peak at the lowest frequency, suggesting a slower variation in resistance due to the lateral nature of wave interaction. Notably, the following wave exhibits the highest magnitude in the response spectrum, highlighting a greater accumulation of wave energy acting along the direction of motion. This suggests that, although the frequency is lower, the sustained interaction with following waves contributes to a more pronounced resistance response overall. As the wave height increases, the peak frequency of the resistance force spectrum decreases.

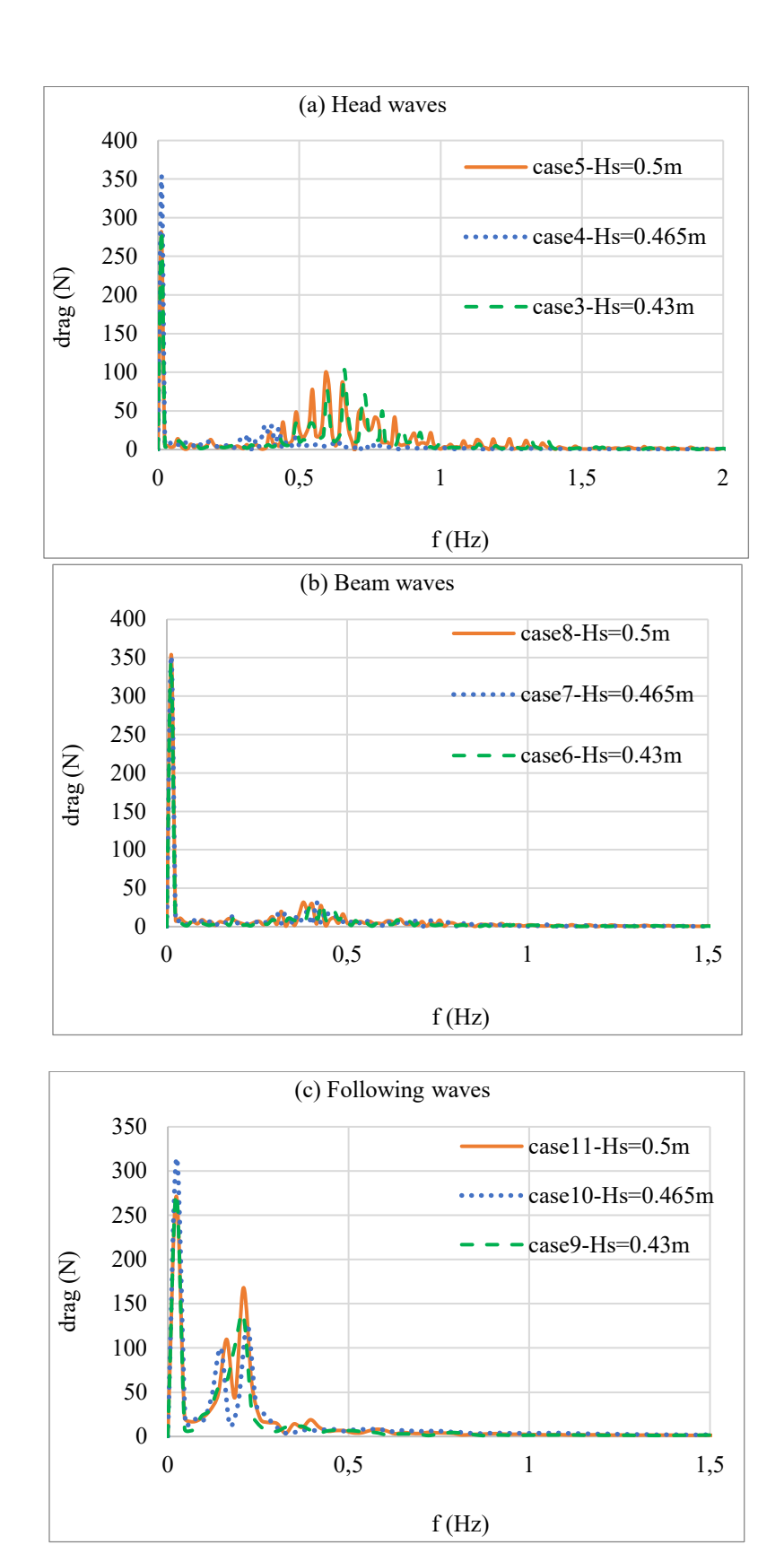
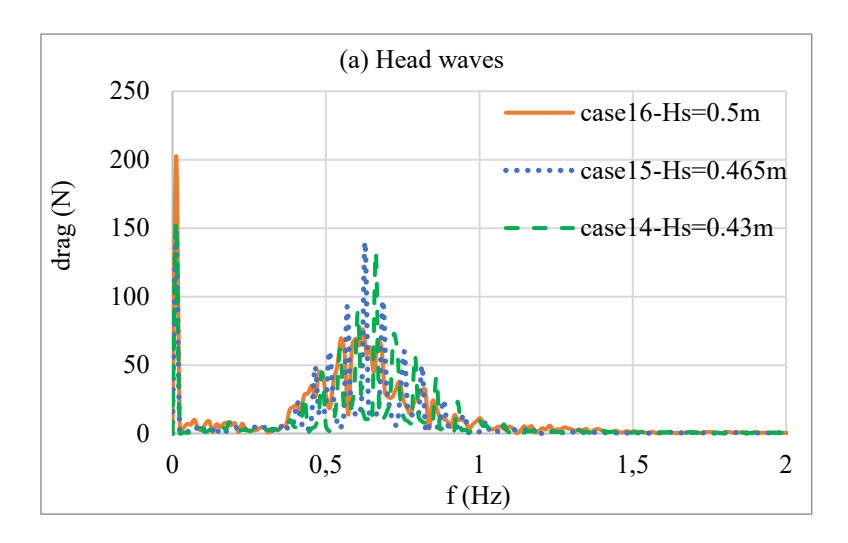


Figure 25. Frequency spectra of submarine resistance at different wave heading angles and and significant wave heights (Hs) in surface mode: (a) Head waves, (b) Beam waves, (c) Following waves.

Figure 25 presents the frequency domain spectrum of the resistance force for the submarine in the submerged mode, under various wave headings and significant wave heights. While the overall response trends remain consistent with those observed in the surface mode, the spectral magnitudes are generally lower in the submerged condition. This reduction can be attributed to the diminished influence of surface wave effects when the submarine is fully immersed. Despite being surrounded entirely by viscous flow, the results indicate that wave-induced forces play a more dominant role in resistance than viscous effects near the free surface.



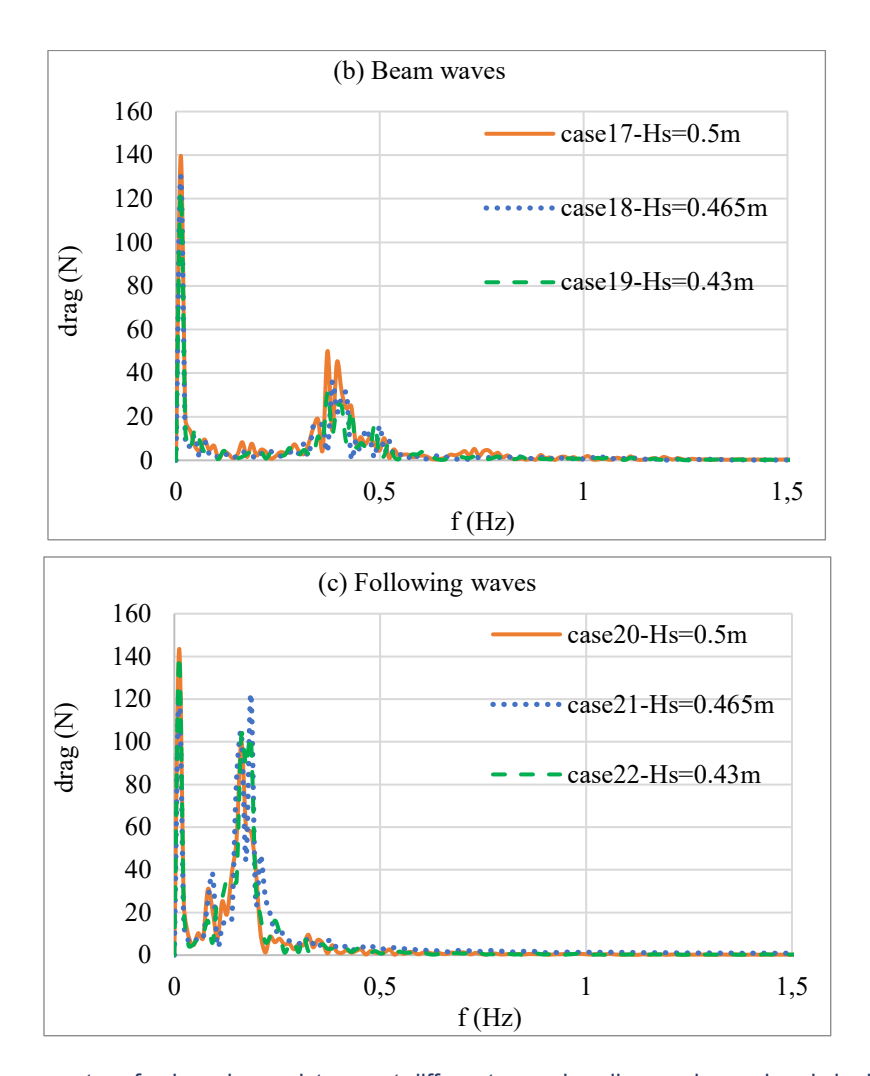


Figure 26. Frequency spectra of submarine resistance at different wave heading angles and and significant wave heights (Hs) in submerged mode: (a) Head waves, (b) Beam waves, (c) Following waves.

5. CONCLUSIONS

This paper originally investigated submarine motion behavior and resistance force at different wave headings using the CFD numerical method. The CFD calculations were performed with STAR CCM+ software, which employs a RANS solver, finite volume method (FVM), overset grid techniques, and the VOF model. The study also provides useful guidance for submarine safety performance when encountering different wave headings. The main results obtained in this study are as follows:

- Heave Motion: Heave motion oscillations are more pronounced in the surface mode than in the submerged mode. In the submerged mode, the buoyancy force and weight remain constant, whereas in the surface mode, buoyancy changes with the heave motion. This results in greater oscillations of heave motion in the surface mode.
- Pitch Motion: In the submerged mode, the amplitude of pitch motion increases compared to the surface mode. This occurs because in the surface mode, the longitudinal metacentric height is above the water surface, whereas in the submerged mode, the longitudinal metacentric point nearly coincides with the center of buoyancy. As a result, the restoring moment for pitch motion in the submerged mode is reduced. Despite the wave effect being less pronounced in the submerged mode, the reduced 36

restoring moment leads to an increase in pitch motion amplitude. The largest pitch response occurs in the following wave.

- Roll Motion: The largest roll response occurs in beam waves. In the surface mode, the amplitude of
 roll motions is greater than in the submerged mode. The transverse metacentric length and restoring
 moment remain constant in both modes. Although the wave effect in the submerged mode is smaller
 than in the surface mode, the amplitude of roll motion still increases in the surface mode.
- Resistance Force: In the surface mode, the resistance force is higher than in the submerged mode. This is primarily due to the wave drag at the water surface. The pitch motion influences the pressure drag, with an increase in pitch angle leading to higher pressure resistance. The increased freedom of motion consequently raises the drag force. While the amplitude of pitch motion is smaller in the surface mode compared to the submerged mode, the increase in wave resistance in the surface mode outweighs the reduction in pressure resistance. As a result, the total resistance is greater in the surface mode.
- Buoyancy and Stability Considerations: In the submerged mode, the center of buoyancy serves as both the longitudinal and transverse metacenter. For ships, the height of the longitudinal metacenter is typically higher than the transverse metacenter, making transverse stability more important. However, for submarines underwater, longitudinal stability is more critical because the longitudinal and transverse metacentric heights are similar, but longitudinal moments are much larger than transverse moments. When the submarine is on the water surface, the transverse metacenter is fixed, but the longitudinal metacenter is not, due to changes in the draft plate as the submarine rotates longitudinally. Below the surface, the longitudinal and transverse metacenters coincide. Consequently, the amplitude of roll motion is greater in the submerged mode.

Conflict of interest: Authors certify that there is no conflict of interest with any financial organization regarding the material discussed in the manuscript.

References

AMIRI, M. M., ESPERANÇA, P. T., VITOLA, M. A. & SPHAIER, S. H. 2018. How does the free surface affect the hydrodynamics of a shallowly submerged submarine? Applied ocean research, 76, 34-50.

AMIRI, M. M., ESPERANÇA, P. T., VITOLA, M. A. & SPHAIER, S. H. 2019. URANS investigation of the interaction between the free surface and a shallowly submerged underwater vehicle at steady drift. Applied Ocean Research, 84, 192-205.

AMIRI, M. M., ESPERANÇA, P. T., VITOLA, M. A. & SPHAIER, S. H. 2020. An initial evaluation of the free surface effect on the maneuverability of underwater vehicles. Ocean Engineering, 196, 106851.

BI, X., SHEN, H., ZHOU, J. & SU, Y. 2019. Numerical analysis of the influence of fixed hydrofoil installation position on seakeeping of the planing craft. Applied Ocean Research, 90, 101863.

CARRICA, P. M., KIM, Y. & MARTIN, J. E. 2019. Near-surface self propulsion of a generic submarine in calm water and waves. Ocean Engineering, 183, 87-105.

CD-ADAPCO 2020. User Guide STAR-CCM+ Version 15.02. 10.04 ed ed.

CHOI, J. & YOON, S. B. 2009. Numerical simulations using momentum source wave-maker applied to RANS equation model. Coastal Engineering, 56, 1043-1060.

DONG, K., WANG, X., ZHANG, D., LIU, L. & FENG, D. 2022. CFD research on the hydrodynamic performance of submarine sailing near the free surface with long-crested waves. Journal of Marine Science and Engineering, 10, 90.

EÇA, L. & HOEKSTRA, M. 2009. Evaluation of numerical error estimation based on grid refinement studies with the method of the manufactured solutions. Computers & Fluids, 38, 1580-1591.

FERZIGER, J. H., PERIĆ, M. & STREET, R. L. 2019. Computational methods for fluid dynamics, springer.

GAO, Z. & SHI, Z. 2023. Numerical study on damaged ship rolling and capsizing in irregular beam waves during quasi-steady flooding. Ocean Engineering, 289, 116308.

GROVES, N. C., HUANG, T. T. & CHANG, M. S. 1989. Geometric characteristics of DARPA (Defense Advanced Research Projects Agency) SUBOFF models (DTRC model numbers 5470 and 5471). David Taylor Research Center Bethesda MD Ship Hydromechanics Dept.

HAN, K., CHENG, X., LIU, Z., HUANG, C., CHANG, H., YAO, J. & TAN, K. 2021. Six-DOF CFD simulations of underwater vehicle operating underwater turning maneuvers. Journal of Marine Science and Engineering, 9, 1451.

HIRT, C. W. & NICHOLS, B. D. 1981. Volume of fluid (VOF) method for the dynamics of free boundaries. Journal of computational physics, 39, 201-225.

HOU, X.-R. & ZOU, Z.-J. 2016. Parameter identification of nonlinear roll motion equation for floating structures in irregular waves. Applied Ocean Research, 55, 66-75.

HUANG, S., JIAO, J. & CHEN, C. 2021. CFD prediction of ship seakeeping behavior in bi-directional cross wave compared with in unidirectional regular wave. Applied Ocean Research, 107, 102426.

ITTC. Recommended procedures and guidelines, Resistance Test. 26th ITTC Resistance Committee, 7.5-02-02-01, 2011.

JAGADEESH, P. & MURALI, K. 2010. RANS predictions of free surface effects on axisymmetric underwater body. Engineering Applications of Computational Fluid Mechanics, 4, 301-313.

JIAO, J. & HUANG, S. 2020. CFD simulation of ship seakeeping performance and slamming loads in bi-directional cross wave. Journal of Marine Science and Engineering, 8, 312.

KIM, D., SONG, S., SANT, T., DEMIREL, Y. K. & TEZDOGAN, T. 2022. Nonlinear URANS model for evaluating course keeping and turning capabilities of a vessel with propulsion system failure in waves. International journal of naval architecture and ocean engineering, 14, 100425.

KIM, S. P. 2011. CFD as a seakeeping tool for ship design. International Journal of Naval Architecture and Ocean Engineering, 3, 65-71.

LATEB, M., MASSON, C., STATHOPOULOS, T. & BÉDARD, C. 2013. Comparison of various types of k–ε models for pollutant emissions around a two-building configuration. Journal of Wind Engineering and Industrial Aerodynamics, 115, 9-21.

LAU, C.-Y., ALI-LAVROFF, J., HOLLOWAY, D. S., SHABANI, B., MEHR, J. A. & THOMAS, G. 2022. Influence of an active T-foil on motions and passenger comfort of a large high-speed wave-piercing catamaran based on sea trials. Journal of Marine Science and Technology, 27, 856-872.

LEE, C.-M., PARK, S.-C., YU, J.-W., CHOI, J.-E. & LEE, I. 2019. Effects of diffraction in regular head waves on added resistance and wake using CFD. International Journal of Naval Architecture and Ocean Engineering, 11, 736-749.

LI, D., YANG, Q., ZHAI, L., WANG, Z. & HE, C.-L. 2021. Numerical investigation on the wave interferences of submerged bodies operating near the free surface. International Journal of Naval Architecture and Ocean Engineering, 13, 65-74.

LIAO, X., CHEN, Z., GUI, H. & DU, M. 2021. CFD prediction of ship seakeeping and slamming behaviors of a trimaran in oblique regular waves. Journal of Marine Science and Engineering, 9, 1151.

LING, X., LEONG, Z. Q., CHIN, C., WOODWARD, M. & DUFFY, J. 2022. Comparisons between seabed and free surface effects on underwater vehicle hydrodynamics. International Journal of Naval Architecture and Ocean Engineering, 100482.

MANSOORZADEH, S. & JAVANMARD, E. 2014. An investigation of free surface effects on drag and lift coefficients of an autonomous underwater vehicle (AUV) using computational and experimental fluid dynamics methods. Journal of Fluids and Structures, 51, 161-171.

NEMATOLLAHI, A., DADVAND, A. & DAWOODIAN, M. 2015. An axisymmetric underwater vehicle-free surface interaction: A numerical study. Ocean Engineering, 96, 205-214.

OZTURK, D., DELEN, C., MANCINI, S., SERIFOGLU, M. O. & HIZARCI, T. 2021. Full-scale CFD analysis of double-m craft seakeeping performance in regular head waves. Journal of Marine Science and Engineering, 9, 504.

QI, X., MIAO, A. & WAN, D. 2018. CFD calculation of hydrodynamic derivatives of underwater vehicle. Chin. J. Hydrodyn, 33, 297-304.

ROACHE, P. J. 1997. Quantification of uncertainty in computational fluid dynamics. Annual review of fluid Mechanics, 29, 123-160.

ROMANOWSKI, A., TEZDOGAN, T. & TURAN, O. 2019. Development of a CFD methodology for the numerical simulation of irregular seastates. Ocean Engineering, 192, 106530. SAOUT, O. & ANANTHAKRISHNAN, P. 2011. Hydrodynamic and dynamic analysis to determine the directional stability of an underwater vehicle near a free surface. Applied Ocean Research, 33, 158-167.

SEO, J. H., SEOL, D. M., LEE, J. H. & RHEE, S. H. 2010. Flexible CFD meshing strategy for prediction of ship resistance and propulsion performance. International Journal of Naval Architecture and Ocean Engineering, 2, 139-145.

SHARIATI, S. K. & MOUSAVIZADEGAN, S. H. 2017. The effect of appendages on the hydrodynamic characteristics of an underwater vehicle near the free surface. Applied Ocean Research, 67, 31-43.

SHIVACHEV, E., KHORASANCHI, M., DAY, S. & TURAN, O. 2020. Impact of trim on added resistance of KRISO container ship (KCS) in head waves: An experimental and numerical study. Ocean Engineering, 211, 107594.

SIGMUND, S. & EL MOCTAR, O. 2018. Numerical and experimental investigation of added resistance of different ship types in short and long waves. Ocean Engineering, 147, 51-67.

STERN, F., WILSON, R. & SHAO, J. 2006. Quantitative V&V of CFD simulations and certification of CFD codes. International journal for numerical methods in fluids, 50, 1335-1355.

SU, Y., WANG, J., ZHUANG, J., SHEN, H. & BI, X. 2021. Experiments and CFD of a variable-structure boat with retractable twin side-hulls: Seakeeping in waves. Ocean Engineering, 235, 109358.

SUN, X., YAO, C., XIONG, Y. & YE, Q. 2017. Numerical and experimental study on seakeeping performance of a swath vehicle in head waves. Applied Ocean Research, 68, 262-275.

TIAN, W., SONG, B. & DING, H. 2019. Numerical research on the influence of surface waves on the hydrodynamic performance of an AUV. Ocean Engineering, 183, 40-56.

WANG, L., MARTIN, J. E., FELLI, M. & CARRICA, P. M. 2020. Experiments and CFD for the propeller wake of a generic submarine operating near the surface. Ocean Engineering, 206, 107304.

WILSON-HAFFENDEN, S., RENILSON, M., RANMUTHUGALA, D. & DAWSON, E. 2009. An investigation into the wave making resistance of a submarine travelling below the free surface. Australian Maritime College, Launceston.

ZAN, Y., LI, Z., LI, F., QIN, L., HUANG, F. & QI, B. 2025. Dynamic characteristics of subsea structures being lifted out of water in irregular waves. Ocean Engineering, 328, 121044.

ZHANG, Z., ZHANG, X., ZHANG, H., BU, S. & ZOU, Z. 2024. Numerical evaluation of turning performance of ships in regular and long-crested irregular waves. Ocean Engineering, 308, 118201.